






Cite this: *Nanoscale*, 2025, **17**, 20231

Self-assembled amino acid-based copolymer nanoparticles for wound healing and tissue regeneration: structure studied through molecular dynamic simulation

Sukanya Patra,^a Desh Deepak Yadav,^a Gurmeet Singh,^a Jyotirmayee,^b Prakriti Sundar Samanta,^a Divya Pareek,^a Aman Srikant Kudada,^a Anjali Ramsabad Mourya,^a ^a Debdip Bhandary *^c and Pradip Paik *^a

Amino acid-based block copolymer nanoparticles with cross-linkers have garnered growing interest in recent years. However, its intricate synthesis and purification difficulties, along with stability concerns linked to intermicellar crosslinking, restrict their potential use in healthcare and therapeutic applications. Thus, the present work aimed to design amphiphilic block copolymer nanoparticles of *N*-acryloyl glycine and *N*-acryloyl-(*L*-phenylalanine methyl ester), *i.e.*, p(NAG-co-NAPA)_{WC}, without the use of a crosslinker via miniemulsion free radical polymerization. The self-assembled π - π stacking structural arrangement of the copolymer at different temperatures has been confirmed through molecular dynamics (MD) simulations, which corroborated the structural stability of the copolymer nanoparticles at physiological temperature (37 °C). The cell migration results of the p(NAG-co-NAPA)_{WC} nanoparticles are complementary to those of the CEMA assay, revealing their tissue regeneration properties. Furthermore, the *in vivo* wound healing study demonstrated that within 13 days post-treatment, ~97% of the wound can be healed, whereas for the control, it was found to be only ~80%. Additionally, the RT-PCR results revealed that the p(NAG-co-NAPA)_{WC} nanoparticles possess anti-inflammatory and tissue regeneration properties by downregulating TNF- α and IL-1 β and upregulating PECAM-1 and VEGF-A, respectively. In conclusion, these p(NAG-co-NAPA)_{WC} nanoparticles are paramount with an extensive clinical potential for the regeneration of acute wounds and can be used for other therapeutic applications.

Received 20th January 2025,
Accepted 29th July 2025

DOI: 10.1039/d5nr00281h

rsc.li/nanoscale

Introduction

Amino acid-based random block copolymers have gained much attention in biomedical applications due to their unique structures and molecular properties. Block copolymers can be self-assembled into various stable nano-objects based on the applied conditions.^{1,2} They can be conjugated with biomolecules, such as drugs or genetic materials, or encapsulated through absorption/adsorption or chemical reactions on their surface or in the void space.^{3,4} Their biocompatibility and high bioavailability have received considerable attention over other properties.⁵ The presence of hydrophilic/hydrophobic functional groups in the polymer chains facilitates the smart

attachment of other multiple blocks, which subsequently helps in developing surface multi-functionality, high cross-linking, interlocking or branching structure, excellent solubility and a symmetric effect. Furthermore, the degradation of their secondary bonds causes pore formation, which may exert influences by varying the temperature, humidity, solvent and pH.⁶

Self-assembly, hydrothermal synthesis, phase separation, reversed atom transfer radical polymerization, and mini/macro emulsion radical polymerizations are often used to synthesize polymer nanoparticles. Crosslinkers play a major role in minimizing premature disintegration and providing prolonged circulation time with the controlled release of biomolecules.^{7,8} Polymeric nanoparticles with chemically bonded crosslinkers are more stable in high dilutions due to their complex interconnected network. However, they show poor response to any external stimuli and self-healing. Excessive use of crosslinkers makes the polymeric particle rigid and can cause severe toxicity to organs.⁹ Furthermore, crosslinkers are highly chemically active and tend to bind with the endothelial cells, body

^aSchool of Biomedical Engineering, Indian Institute of Technology (BHU) Varanasi, Uttar Pradesh, 221 005, India. E-mail: paik.bme@iitbhu.ac.in

^bSchool of Biotechnology, Institute of Science, Banaras Hindu University, Varanasi, 221 005 Uttar Pradesh, India

^cDepartment of Chemical Engineering and Technology, Indian Institute of Technology (BHU) Varanasi, Uttar Pradesh, 221 005, India. E-mail: debdip.che@iitbhu.ac.in



proteins, metal ions, enzymes and lipids.^{10,11} There are major challenges with crosslinkers as they can hinder systematic cellular activities.¹² Due to these limitations, a series of chemically synthesized covalently crosslinked nanoparticles are restricted from clinical trials.¹³ On the other hand, non-covalently cross-linked polymeric nanoparticles are often favoured due to their dynamic evolution and ease of preparation.^{14,15} The stability of the non-covalent crosslinked nanoparticles arises due to their hydrogen bonds, dipole-dipole interactions, π - π stacking, coordination complexing, and hydrophilic or hydrophobic interactions.¹⁶ Double hydrophilic block copolymers of PEG-*b*-PNIPAM were synthesized following RAFT polymerization based on hydrogen bonds.¹⁷ Similarly, phenylboronic acid-modified-PEG-*b*-P(Asp-co-AspPBA) was synthesized through the ROP approach to encapsulate insulin from the attack of external proteases, which was stabilized by hydrophobic interactions.¹⁸ However, in both cases, the presence of PNIPAM limits their extensive use in therapy. Compared to all other secondary interactions, π - π stacking provided more stability to the polymeric nanoparticles despite the presence of weak interactions. The π - π stacking is a spatial arrangement of phenyl rings that usually exists between two molecules that are deficient or abundant with electrons. The π - π stacking-based polymer micelles showed improved loading and delivery of hydrophobic drugs containing aromatic groups to tumors, and a significant decrease in CMC.¹⁹ The self-assembled polymeric nanoparticles supported by physical crosslinkers are often reversible and dynamic.²⁰ To enhance the noncovalent interactions and higher stability, self-assembled polymeric nanoparticles can be composed of both hydrophilic and hydrophobic units.²¹ It should be noted that the potential therapeutic applications of non-covalently crosslinked, self-assembled amino acid-based block copolymers have yet to be explored.

In the above description, the small size of the 'NAG' unit and the presence of a phenyl ring in the 'NAPA' unit motivated us to design a random di-block copolymer of *N*-acryloyl glycine (NAG) and *N*-acryloyl-(*L*-phenylalanine methyl ester) (NAPA), p(NAG-co-NAPA)_{wc} via non-covalent crosslinking for biomedical applications. The self-assembly nature of the polymer chains can form the nanoparticles without the use of additional crosslinkers. Considering this, the self-assembled nature of NAPA-NAG at different temperatures has been explored through molecular dynamics (MD) simulation. The atomistically modelled p(NAG-co-NAPA)_{wc} revealed its internal properties via MD simulations. A total of 500 dimer units of NAPA-NAG (as obtained from MALDI-ToF results) were inserted randomly and solvated with water within an orthogonal periodic box, and allowed to evolve for 100 ns. The effect of the temperature on the molecular morphology of the dimers while forming self-assembled copolymer nanoparticles was studied in detail. Through the MD simulation, we further delved into the analysis of the structure of the agglomerates at different temperatures by studying the radial distribution functions between critical pairs. We also investigated how the interconnected network-like molecular morphology is formed. This

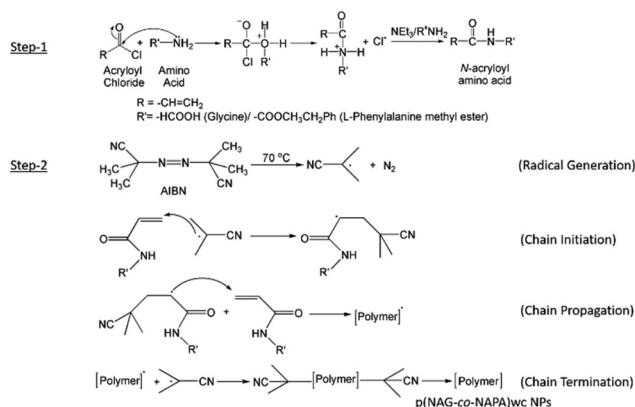
morphology has been predicted in the presence of carboxylic and amide groups that can interact with water and help to stabilize the self-assembled polymeric nanostructures by electrostatic interactions. It should be noted that the surface potential can also promote the exposure of these groups present on the surface of the nanoparticles. Hence, a MD simulation study has been employed to study the colloidal stability of such copolymer nanoparticles.

NAG and NAPA monomers are highly soluble in organic solvents, and their copolymers are well known for their wide applications in healthcare as therapeutics.^{22,23} Therefore, the hemocompatibility and cytocompatibility of p(NAG-co-NAPA)_{wc} nanoparticles have been studied against rat RBCs and L929 (mouse fibroblast), respectively, and their potential use in wound healing has been investigated through the scratch wound assay and CEMA assay. The present study further investigated the irritation and sensitization, levels of pro-inflammatory cytokines, and the relative fold change in gene expressions of the p(NAG-co-NAPA)_{wc} nanoformulation in *in vivo* wound healing using rats.

Results

Synthesis and characterization of monomers (NAG and NAPA) and random block copolymer nanoparticles (p(NAG-co-NAPA)_{wc})

p(NAG-co-NAPA)_{wc} was synthesized in two steps. The first step was the synthesis of the monomers (NAG and NAPA) (Scheme 1 (Step-1)), which was followed by the synthesis of the copolymer nanoparticles (Scheme 1 (Step-2)). The monomer synthesis was carried out using the Schotten-Baumann reaction, where the amine group of amino acids reacts with acryloyl chloride in an alkaline medium to form an amide bond.^{3,23} The characteristic FTIR and NMR (¹H and ¹³C) bands for both monomers are shown in Fig. S1-S3. For the synthesis of the copolymer p(NAG-co-NAPA)_{wc} nanoparticles, the free radical mini-emulsion polymerization method was followed in



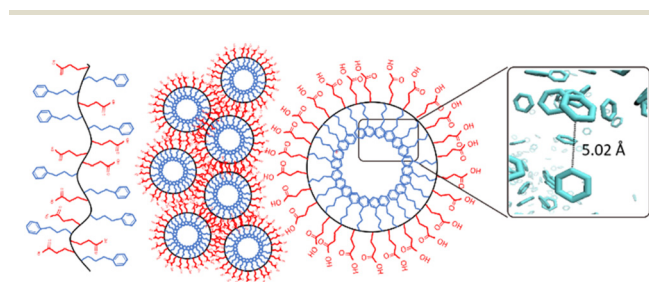
Scheme 1 Schematic of the mechanism involved in the synthesis of NAG (Step-1), NAPA (Step-1) and p(NAG-co-NAPA)_{wc} nanoparticles (Step-2).



accordance with a previously reported synthesis method (Scheme 1, Step-3) with slight modification, *i.e.*, avoiding the use of a crosslinker (divinylbenzene).³ In the synthesis procedure of the p(NAG-*co*-NAPA)_{wc} nanoparticles, hexadecane (HD) was used as a co-stabilizer to increase the stability of the droplets formed in the emulsion process to prevent coagulation of the particles. Both monomers were dispersed in the oil phase (toluene), and monomer droplets were formed. The radical initiator AIBN allows for the initiation of the polymerization reaction at 65 °C–75 °C within the oil/monomer droplet, and at the interface of the oil/monomer droplets and aqueous phase. The oily core surrounded by a thin polymeric membrane was stabilized by crosslinking the monomer droplets with NAG, which can generate pores in the nanoparticles. The NAG-to-NAPA wt% ratio remained constant (*i.e.*, 50:50) throughout the reaction process. SDS was used as an emulsifier. Nanoparticle synthesis without SDS causes a decrease in stability and forms aggregates during synthesis. The mechanism behind this copolymer synthesis is simple and straightforward. In brief, AIBN first initiates the reaction by attacking the hydrogen attached to the terminal sp²-hybridized primary carbon of NAG and NAPA, and forms radical ions of both monomers. Then, these radicals propagate the chain and eventually the chain undergoes termination, where different growing chains meet 'head-to-head' by forming a π -bond (Scheme 2). The formed copolymer p(NAG-*co*-NAPA)_{wc} is amphiphilic in nature, *i.e.*, the carboxylic acid group (–COOH) in NAG and one phenyl ring present in NAPA provide hydrophilic and hydrophobic properties to the whole system, respectively. They form a self-assembled structure by moving phenyl rings towards the core of the micelle and carboxylic groups towards the outer side of the micelle. This arrangement of phenyl rings is facilitated by the electrostatic intramolecular π - π stacking among phenyl groups, as reported by Hunter and Sanders in 1990.²⁴ Thus, this arrangement helps in generating a network-like copolymer without the use of any crosslinkers, and it promotes the stabilization of the NPs through molecular packing.²⁵

Furthermore, the chemical functionalities of the p(NAG-*co*-NAPA)_{wc} nanoparticles were confirmed through ¹H NMR, ¹³C NMR and FTIR, and the molecular weight was estimated through MALDI-TOF MS. The position and number of hydro-

gen atoms present in the p(NAG-*co*-NAPA)_{wc} nanoparticles were confirmed through ¹H and ¹³C NMR. The important bands are designated as follows: ¹H NMR (ppm): δ = 8.15 (1H, d, (secondary amine of the NAG monomer)), 7.25 (1H, d, (secondary amine of the NAPA monomer)), 7.15 (5H, m, aromatic H), 4.02 (3H, t, alkoxide), 7.05 (–C(=O) N) *cis* and 5.60 (–C(=O) N) *trans*, 3.96–2.37 (1H, m, (–CH₂ adjacent to the amide of the NAG monomer)), 3.21–2.29 (1H, m, (–CH₂ adjacent to amide of the NAPA monomer)) and 2.51 (1H, dd, *J* = 11.3, 9.5) (Fig. 1(a)), ¹³C NMR (ppm): the disappearance of all of the bands for the monomers and only one band at δ ranging from 40.33 to 39.32 shows the splitting of the 2° alkane (Fig. S4) and FTIR (KBr), ν (in cm^{–1}) = 3328 (secondary –NH, s), 3020 (aromatic –CH, s), 2925 and 2863 (alkane –CH, s), 1726 (ester C=O, s), 1649 (–NH–C=O, s), and 739 (aromatic –CH, b) (Fig. 1(b)). The UV-Vis spectra confirm the formation of the p(NAG-*co*-NAPA)_{wc} nanoparticles with the absorption bands appearing at λ_{max} = 220 nm and 258 nm, corresponding to π - π^* and n- π^* transitions, respectively (Fig. S5). The π - π^* transition confirms the presence of the carbonyl group, while the n- π^* transition confirms the presence of double bonds in the p(NAG-*co*-NAPA)_{wc} nanoparticles. MALDI-TOF analysis con-



Scheme 2 Schematic of the p(NAG-*co*-NAPA)_{wc} nanoparticles forming a self-assembled nanostructure via physical crosslinking induced by π - π stacking.

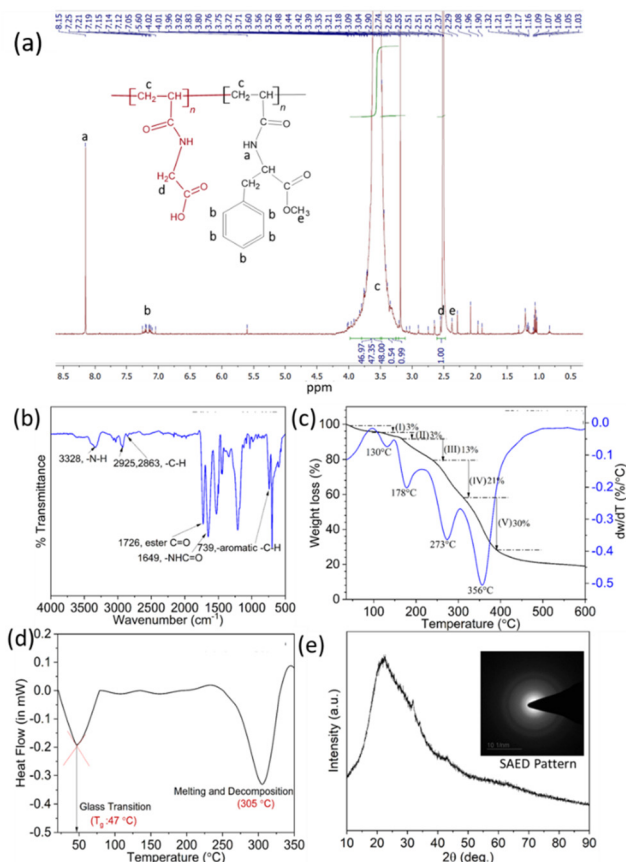


Fig. 1 Physicochemical properties of the p(NAG-*co*-NAPA)_{wc} nanoparticles. (a) ¹H NMR spectra, (b) FTIR spectra, (c) TGA and DTGA thermograms, (d) DSC thermogram and (e) XRD pattern of the p(NAG-*co*-NAPA)_{wc} nanoparticles. The inset image of (e) is the SAED pattern for the p(NAG-*co*-NAPA)_{wc} nanoparticles.

firms the molecular weight of the copolymers ranging from 377 Da to 493 Da, with an intense band at 400.02 Da, which indicates the possibility that most of the fragments are nearly equal to the summation of the individual molecular masses of one NAG and one NAPA unit. Therefore, the highest intensity fragments consist of a dimer of NAG and NAPA. The first highest fragment is obtained at 406.31 (m/z), *i.e.*, number average molecular weight (\overline{M}_n), and 400.02 (m/z), *i.e.*, weight average molecular weight (\overline{M}_w), with a PDI of 0.99 representing the uniform length of polymer chains. The difference between two adjacent peaks varies from 13 Da to 45 Da, which further confirms the formation of random p(NAG-*co*-NAPA)_{wc} copolymer nanoparticles with a heterogeneous population in the system (Fig. S6). Therefore, all these chemical functionality-based observations confirm the successful synthesis of p(NAG-*co*-NAPA)_{wc} nanoparticles.

Thermal stability analysis of the p(NAG-*co*-NAPA)_{wc} nanoparticles exhibits five steps of weight loss ranging from 130 °C to 356 °C (Fig. 1(c)). The thermal stability of the nanoparticles at physiological temperature (37 °C) is crucial for their use in therapeutic applications. The five steps weight loss (%) were observed at the following ranges: (I) 45 °C–108 °C (3%), (II) 108 °C–158 °C (3%), (III) 158 °C–240 °C (13%), (IV) 240 °C–310 °C (21%) and (V) 310 °C–390 °C (30%). Stage I is observed due to the loss of free moisture, and stages II, III, IV, and V are observed due to the thermal degradation of polymer chains. It should be noted that beyond 390 °C, the only remaining materials are the carbon residues. The DTGA plot of the p(NAG-*co*-NAPA)_{wc} nanoparticles (Fig. 1(c)) provides an idea of the degradation temperatures corresponding to each weight loss step. The maximum rates of degradation are found to occur at 130 °C, 178 °C, 273 °C and 356 °C. Any observed degradation at lower temperature may be due to the presence of a low molecular weight of p(NAG-*co*-NAPA)_{wc} in the nanoparticles. Furthermore, to evaluate the thermal phase transition, DSC analysis of the p(NAG-*co*-NAPA)_{wc} nanoparticles was conducted from RT to 350 °C (Fig. 1(d)). The glass transition temperature (T_g) is observed at 47 °C with an endothermic peak (*endo* down). An additional endothermic peak is observed at 305 °C due to the decomposition of the p(NAG-*co*-NAPA)_{wc} nanoparticles. From XRD, it is confirmed that the p(NAG-*co*-NAPA)_{wc} nanoparticles are amorphous in nature, which matches well with the diffused ring of SAED patterns obtained from the HR-TEM image of the p(NAG-*co*-NAPA)_{wc} nanoparticles (Fig. 1(e) and inset image) represented in the subsequent section (Fig. 2(b)). The amorphous nature of p(NAG-*co*-NAPA)_{wc} nanoparticles helps in improving the nanoparticle's apparent bioavailability.^{26,27}

Morphology and colloidal stability of the p(NAG-*co*-NAPA)_{wc} nanoparticles

The shape, size, and morphology of the p(NAG-*co*-NAPA)_{wc} nanoparticles were investigated *via* FESEM, HR-TEM and AFM analysis (Fig. 2). The microscopic images (Fig. 2(a), (b) and (d)) revealed that the p(NAG-*co*-NAPA)_{wc} nanoparticles are spherical in nature with a diameter ranging from 120–400 nm. Fig. 2(e)

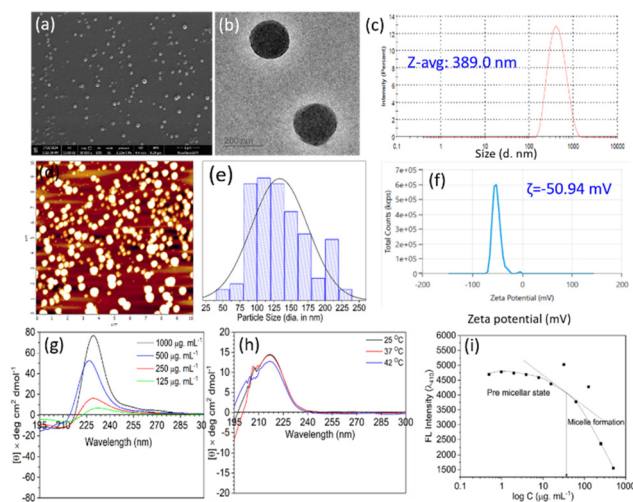


Fig. 2 Size, shape, morphology and colloidal stability of the p(NAG-*co*-NAPA)_{wc} nanoparticles. (a) FESEM, (b) HRTEM image (scale bar: 200 nm), (c) DLS, (d) AFM, (e) particle size distribution obtained from (a), (f) zeta potential, (g) and (h) CD spectra of p(NAG-*co*-NAPA)_{wc} nanoparticles at different concentrations and three different temperatures, respectively, and (i) CMC of the p(NAG-*co*-NAPA)_{wc} nanoparticles.

shows the particle size distribution (120–200 nm) obtained from the FESEM images. From the HR-TEM images (Fig. 2(b)), the size was calculated to be 200–220 nm in diameter. From AFM, the size is calculated to be 200–300 nm in diameter. The variation in the sizes of the p(NAG-*co*-NAPA)_{wc} nanoparticles obtained from different microscopy results is due to the different modes of the experimental procedure. However, the dark core-like structure observed in Fig. 2(b) is due to the self-assembly nature of the polymer chains of the p(NAG-*co*-NAPA)_{wc} nanoparticles, as shown in Scheme 2. This self-assembly occurs due to the presence of hydrophilic carboxylic groups on the surface of the particle, which form a corona, and hydrophobic phenyl rings present inside the shell. The hydrophobic rings are arranged in a T-shaped π stacking configuration (Scheme 2). A MD simulation study has been performed to confirm the self-assembly structure of the p(NAG-*co*-NAPA)_{wc} polymer chains in nanoparticles, which is discussed in the subsequent section. Furthermore, the colloidal stability of the p(NAG-*co*-NAPA)_{wc} nanoparticles was examined by DLS in Milli-Q water at RT (Fig. 2(c)). The hydrodynamic diameter is calculated from the size distribution by intensity plot, and the Z-average is found to be 389 nm with 0.171 PDI. Furthermore, the volume distribution by intensity report and combined plot of the intensity *vs.* size and volume *vs.* size are shown in Fig. S7. The observation of a larger size for the p(NAG-*co*-NAPA)_{wc} nanoparticles is due to the entrapment of water molecules in the copolymers' network and possible swelling of the nanoparticles.

The zeta potential was calculated to be –50.94 mV, which comprises the colloidal stability of the p(NAG-*co*-NAPA)_{wc} nanoparticles (Fig. 2(f)). The optical properties of the p(NAG-*co*-NAPA)_{wc} nanoparticles were confirmed through CD spec-



troscopy, as mentioned in the Experimental section with concentrations of 1000 to 125 $\mu\text{g mL}^{-1}$ at 25 $^{\circ}\text{C}$. At all concentrations, a distinct narrow CD band appeared at $\lambda_{\text{max}} = (230 \pm 5)$ nm (Fig. 2(g)) due to the presence of optically active NAPA monomer in the copolymer nanoparticles.²⁸ As reported earlier, the intensity of the CD spectra increases with an increase in the concentration of nanoparticles (*i.e.*, subsequently, an increase in the concentration of the NAPA monomer). From Fig. 2(g), it is evident that the formation of a self-assembled structure occurs in the medium as the positive and negative bands are separated from each other.²⁹ Furthermore, with the concentration of the p(NAG-co-NAPA)_{wc} nanoparticles fixed at 125 $\mu\text{g mL}^{-1}$, the CD spectra were recorded at three different temperatures (25 $^{\circ}\text{C}$, 37 $^{\circ}\text{C}$ and 42 $^{\circ}\text{C}$) (Fig. 2(h)). Similar CD spectra were obtained for each temperature with $\lambda_{\text{max}} = 218$ nm, which comprises the existence of a secondary structure of the polymer chains in the copolymer nanoparticles. Using JASCO software, it was identified that the copolymer consists of $\sim 100\%$ turn-type secondary arrangements formed in the polymeric particles, with a few numbers of small loops consisting of hydrogen bonds (Fig. S8). These features assist the formation of fibrils like structural arrangement in the copolymer nanoparticle.³⁰ Subsequently, these secondary structures can help in understanding the interactions between nanoparticles and drug molecules. This can further assist in the design of a drug or vaccine with desired stability, shelf-life, and efficacy of treatment. The CMC is an important parameter in colloid chemistry, which denotes the minimum concentration needed to form a self-assembled structure of nanoparticles in the liquid medium. The magnitude of the CMC is closely related to the size of the nanoparticle and hydrophobic block present in the system. It should be noted that a block copolymer is biocompatible, and a precise ratio should be maintained between hydrophobic and hydrophilic units for its effective use in therapy.^{31,32} Herein, the CMC value for the p(NAG-co-NAPA)_{wc} nanoparticles was calculated to be 1.56 $\mu\text{g mL}^{-1}$ (Fig. 2(i)). This low CMC value demonstrated that a good hydrophobic to hydrophilic ratio is maintained in the system with the increase in the extent of π - π stacking due to the physical crosslinking. The MD simulation results also demonstrate that the benzene rings are present in close proximity with a distance of 5.02 Å (Scheme 2). This leads to the formation of aggregates of p(NAG-co-NAPA)_{wc} nanoparticles in the particular medium or solvent. Furthermore, such systems with low CMC can tolerate the high degree of dilution, *i.e.*, bloodstream dilution, and makes the nanoparticles biologically and mechanically more stable. The physical crosslinking can reform the nanoparticles even after disintegration of the self-assembly structure, which is known as self-healing of nanoparticles.^{33,34}

Molecular aggregation of p(NAG-co-NAPA)_{wc} nanoparticles

Molecular dynamics simulations of atomistically modelled p(NAG-co-NAPA)_{wc} molecules revealed the molecular organization in the presence of water. 500 dimers of NAG-co-NAPA were randomly inserted within an orthogonal periodic simu-

lation box, followed by solvation with water. The aqueous solution of NAPA-NAG, having a concentration of 0.2 g mL^{-1} , was allowed to evolve for 100 ns. The concentration of the dimer in the simulations is much higher compared to the concentration range used in the experiments (7.8–1000 $\mu\text{g mL}^{-1}$). To prepare the computational systems with concentrations in this range, the number of solvent molecules in the simulation box would have to be very large (more than 200 times the present), and the computation would be extremely expensive and time-consuming.

Fig. 3 shows the evolution of dimer molecules in solution to reveal their organization and their structural properties at three different temperatures (298 K, 310 K and 315 K). The initial configurations shown in Fig. 3(a, e, and i) indicated that the dimer molecules (different colours for different molecules) are randomly distributed in the water medium (not shown for clarity). From the snapshots in the top row of Fig. 3, it is evident that the dimer molecules are forming interconnected aggregates (indicated by continuous surfaces with multiple colours) spreading over the whole simulation box. Additionally, Fig. 3(c) and (d) indicate that the interconnected aggregates evolved their structure with time. However, the interconnected aggregates are building up the walls of the porous structure, as observed in experiments. From Fig. 3(e–f), it is revealed that the NAG-co-NAPA dimer molecules are also forming interconnected structures at 25 $^{\circ}\text{C}$ (298 K), which further manifests the porous structure of the nanoparticles obtained in the experiments. As the temperature rises to 37 $^{\circ}\text{C}$ (310 K), the number of interconnected fragments decreases (Fig. 3(g and h)); hence, the porosity in the structure decreases. However, this extent of change is negligible. At 42 $^{\circ}\text{C}$ (315 K) at 40 ns, a distinct agglomeration is observed (Fig. 3(j)) compared to that at 25 $^{\circ}\text{C}$ and 37 $^{\circ}\text{C}$ (Fig. 3(b) and (f)), respectively). However, at 80 ns, a deviation is observed with respect to the previous two cases. This phenomenon is observed as a larger

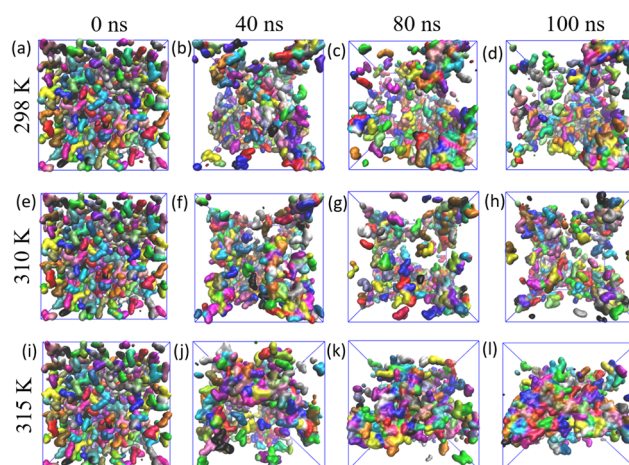


Fig. 3 Structural evolution of NAPA-NAG at three different temperatures (298 K, 310 K and 315 K) at 0, 40, 80 and 100 ns. The dimers are represented by QuickSurf, and other components of the solutions were omitted for visual clarity.



number of agglomerated units were present (Fig. 3(k)), which are surrounded by water molecules. This would lead to the formation of a structure with less porosity. However, until 100 ns (Fig. 3(l)), the structure remained similar. This revealed that there is an impact of temperature on the molecular morphology of dimers while forming nanoparticles. Furthermore, the interconnected network-like molecular morphology of nanoparticles also indicated that the hydrophilic groups (such as carboxylic and amide) are strongly interacting with water molecules and prefer to be exposed to water. These molecular arrangements help in stabilizing the structure of the nanoparticles. The presence of these groups at the surface of nanoparticles justifies the negative zeta potential (Fig. 2(f)) that ensures the colloidal stability of the designed nanoparticles in aqueous medium. Additionally, to establish a better correlation, the aggregation behaviour of the hydrophobic phenyl groups present in the NAPA units and hydrophilic carboxyl groups present in the NAG units after 0, 40 and 80 ns of simulation run in the three concerned temperatures as shown in Fig. S10 and S11.

Structural properties of $p(\text{NAG-co-NAPA})_{\text{wc}}$ molecular assembly

We further delved into the analysis of the structures of the agglomerates at different temperatures through analysis of the radial distribution functions between critical pairs of atoms. In Fig. 4(a–c), the radial distribution function of pairs, such as water-carboxylic, water-phenyl, and water-amine groups are shown at different temperatures. The pair correlation between the carboxyl groups and the water molecules is strong, as indicated by the appearance of the sharp repetitive peaks at regular intervals. However, the local density of the water molecules has not reached to the overall density of the system, comprising the formation of an agglomerated structure (Fig. 3). Another interesting aspect to note here is the drop in the peak intensity with temperature. This observation suggested that the solvation shells gradually become less populated as the temperature rises. The pair correlation between the water and phenyl groups did not pose a sharp peak (Fig. 4(b)), indicating the presence of a structured water layer surrounding the phenyl rings due to the electronic cloud of the phenyl rings. The pair correlations gradually increase towards unity, suggesting the formation of an overall agglomerated structure. In the case of this pair, the number of water molecules present around the phenyl rings also decreased with an increase in the temperature of the system. However, the amide/amine nitrogen atoms showed a stronger affinity with water molecules compared to the phenyl groups, as indicated by the appearance of a sharp peak (Fig. 4(c)). It is also revealed that the amine groups hold the water molecules at ~ 2.8 Å, which allows the formation of hydrogen bonds with the nitrogen atoms. In this case, the peak height is decreased slightly with an increase in temperature. Furthermore, the coordination numbers for 310 K to 315 K are found to be higher in value compared to the temperature range of 298 to 310 K (inset Fig. 4(c)). The interplay between

the hydrophilic and hydrophobic groups has played a key role in the aggregation of copolymers. More specifically, the hydrophobic phenyl groups played a crucial role in agglomeration due to possible π - π stacking. Furthermore, we have calculated the RDF between carbon atoms at the 1 and 4 positions of different phenyl rings, denoted as Ph11, Ph14, and Ph44 (Fig. 4(d)). In this figure, comparisons of RDFs between different pairs are shown at different temperatures. The 4–4 pairs correlation showed a stronger split of peaks at lower distances, whereas the other pairs exhibited weaker peaks at higher distances. This indicated that the 4–4 interactions are much stronger, and thus played a predominant role in agglomerating the dimers. However, the structure is amorphous in nature, as indicated by the absence of any sharp peak. This dominance for Ph44 could be due to its readily accessible position, along with the presence of a bulky group with Ph11. Hence, to avoid steric hindrances, close associations of 4–4 pairs are favoured across all three temperatures, demonstrating a T-shaped π - π stacking.³⁵ Furthermore, the histograms of angle distribution at three different temperatures are provided in Fig. S12. On the other hand, the 1–1-pair correlation exhibited a broader split peak at a longer distance. In contrast, interestingly, the 1–4 pairs showed a crossover of the RDF of two individual pairs. As the temperature of the system increases, all of the RDF peak heights increased and broadened. This indicates that the amorphous nature of the agglomerates increases with the increase in temperature.

Furthermore, to elucidate the behaviour of dimers in the aqueous system, the number of hydrogen bonds plays a pivotal role in aggregation between the dimers and water molecules, which was calculated at all temperatures. The average number of hydrogen bonds formed between dimers is shown in Fig. 4(e). Additionally, the intermolecular hydrogen bonds are predominantly formed. However, the total number of formed hydrogen bonds is approximately five times more than that of the intramolecular hydrogen bonds formed between the carboxylic acid groups and amine groups. The total number of hydrogen bonds increased with the increase in temperature, while the extent of intramolecular binding decreased.

At lower temperatures, due to the presence of a large number of intramolecular hydrogen bonds, a less interconnected hydrogen-bonding network is formed, leading to the inclusion of more water molecules in the agglomerates. However, with the increase in temperature, the molecules assembled themselves into a larger network through the formation of hydrogen bonds, allowing the molecules to agglomerate tightly in an elongated manner. Additionally, the number of hydrogen bonds formed between dimers and water molecules are shown in Fig. S13(a) at three temperatures, which also further demonstrates that with the increase in temperature, there is a sharp decrease in the number of hydrogen bonds. This decrease in the extent of hydrogen bonds matches well with the number of contact results as shown in Fig. S13(b). The end-to-end distribution of the dimers also



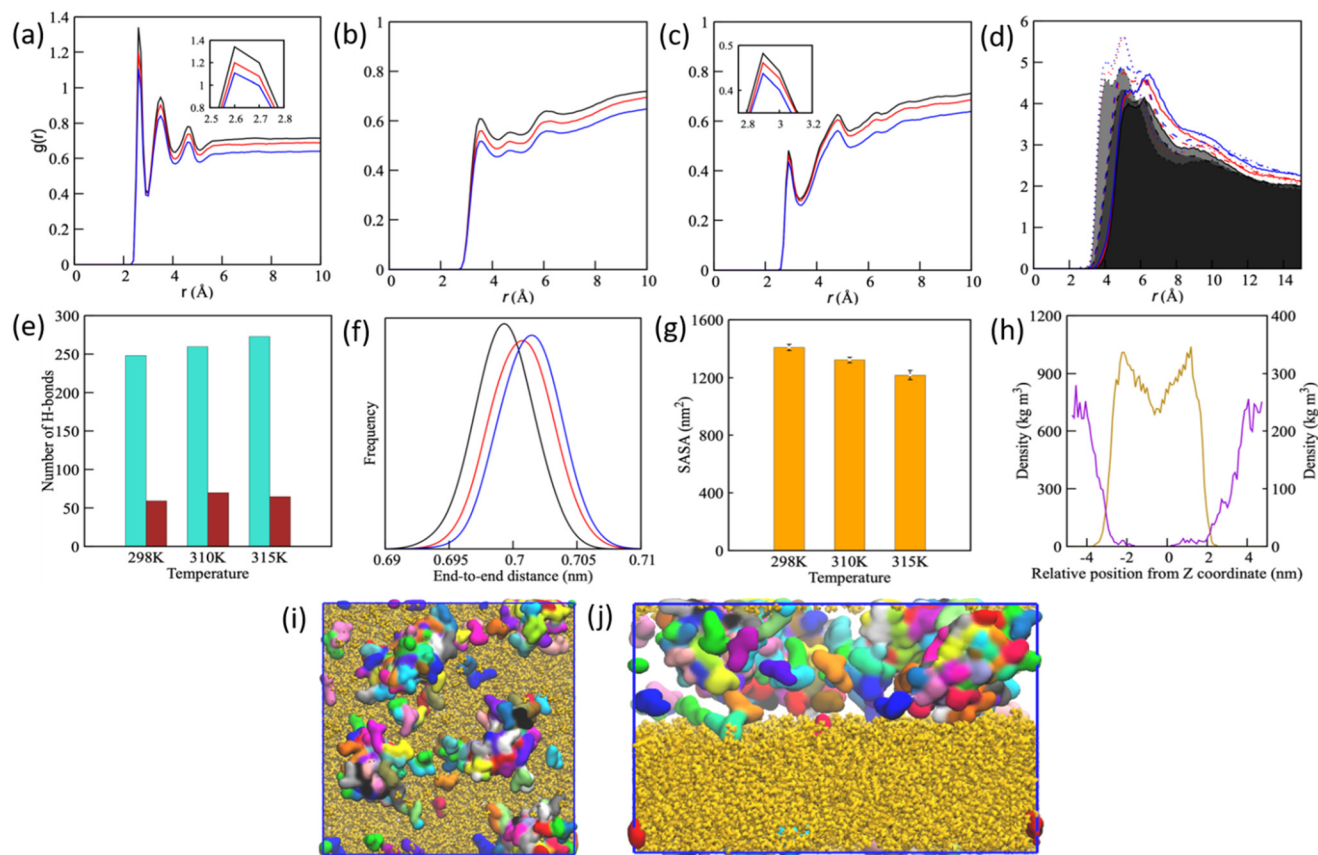


Fig. 4 Radial distribution functions between oxygen atoms in water molecules and (a) the carboxylic groups, (b) phenyl groups, (c) nitrogen atoms in dimers at different temperatures. The black, red and blue lines in the figures represent temperatures, 298, 310 and 315 K, respectively. (d) Radial distribution functions between the phenyl carbon atoms at the 1 and 4 positions at different temperatures. (e) Number of intramolecular hydrogen bonds between $-\text{COO}$ and $-\text{NH}$ atoms with the total number of hydrogen bonds between dimer units at different temperatures. (f) Distribution of end-to-end distance of the dimers at different temperatures. (g) Change in the SASA of the dimers matrix in aqueous solution at different temperatures with the evolution time. (h) Density distribution of the dimer and POPC membrane along the direction perpendicular to the membrane surface. (i and j) Side and top views of agglomerates of dimers in water on the POPC membrane at 310 K.

quantifies the elongation of the molecules, as shown in Fig. 4(f). As the temperature increases, the end-to-end distribution of peaks is shifted towards the right, indicating the formation of a more elongated conformation of the molecules in the agglomerate. Hydrophilicity of the agglomerated structure is a key parameter in utilizing it for therapeutic applications. Thus, we have calculated the solvent accessible surface area (SASA) to quantify it (Fig. 4(g)). It can be seen that with an increase in temperature, SASA decreases, which supports the hydrophobic nature of the agglomerates. A lower SASA value at 315 K hints towards the formation of larger globular aggregates. However, a higher SASA is available at the physiological temperature (310 K). These findings suggest that higher aggregation occurred at higher temperature, and subsequently helps in stabilizing the nanoparticles. The biocompatibility of dimers was also assessed through the interactions with the POPC bilayer membrane at 310 K. The density distribution of dimers shown in Fig. 4(h) was calculated around the z-axis of the membrane, showing that dimer aggregates (Fig. 4(i)) have formed bonds to the membrane within 100 ns.

Furthermore, the dimers formed a close association with the bilayer surface of the membrane, as shown in Fig. 4(j).

Biocompatibility, hemocompatibility, proliferative and migratory behavior of $\text{p(NAG-co-NAPA)}_{\text{wc}}$ nanoparticles through *in vitro* study

Biocompatibility and hemocompatibility are major parameters that need to be studied for any biomedical application of copolymer nanoparticles. Fibroblast cells are abundantly present in mammals. We have selected L929 cells to check the biocompatibility of the developed $\text{p(NAG-co-NAPA)}_{\text{wc}}$ nanoparticles. It can be seen that L929 cells treated with $\text{p(NAG-co-NAPA)}_{\text{wc}}$ nanoparticles demonstrated concentration-dependent proliferative behaviour, and are cytocompatible in nature. Additionally, as the concentration of the $\text{p(NAG-co-NAPA)}_{\text{wc}}$ nanoparticles increases, the cell viability (%) steadily increases. However, from 500 to 1000 $\mu\text{g mL}^{-1}$, the cell viability (%) slowly decreases. This decrease in cell viability (%) is obtained due to the high contact inhibition experienced by cells in the respective confined space for a longer period of



time (24 h). It is worth mentioning that at the $p(\text{NAG-co-NAPA})_{\text{wc}}$ nanoparticle concentrations of 7.8125, 15.625, 31.25, 62.5 and 125 $\mu\text{g mL}^{-1}$, the cell viability (%) are observed to be 137.1 ± 2.3 , 122.9 ± 2.5 , 119.2 ± 1.9 , 119.9 ± 1.2 and 119.3 ± 1.4 , respectively (Fig. 5(a)). These results clearly suggest that the designed $p(\text{NAG-co-NAPA})_{\text{wc}}$ nanoparticles are biocompatible and can promote the proliferation of L929 cells. Furthermore, hemocompatibility is a crucial parameter for nanobiomaterials for their use in therapeutic applications, as the nanoparticles during systemic circulation can cause toxic effects and limit the therapeutic benefits.³⁶ The copolymer should have a hemolysis value below 5% to avoid any toxic effect. Thus, the hemolytic activities of $p(\text{NAG-co-NAPA})_{\text{wc}}$

nanoparticles were studied in both dose- and time-dependent manner over a concentration range of 500 to 7.8125 $\mu\text{g mL}^{-1}$ at 2 and 8 h. Herein, distilled water was considered as a positive control and pure RBC suspension was considered as a negative control. Although a varied degree of hemolysis (%) was observed at the different times for all the concentrations taken in this study, the exhibited hemolysis was calculated to be below 5% (Fig. 5(b)). At 500 $\mu\text{g mL}^{-1}$, hemolysis values are observed to be $8.0\% \pm 1.1\%$ and $10.1\% \pm 1.5\%$ for 2 h and 8 h, respectively (Fig. 5(b)). In conclusion, the $p(\text{NAG-co-NAPA})_{\text{wc}}$ nanoparticles can be considered as a safe biomaterial, and up to 250 $\mu\text{g mL}^{-1}$ can be used for various therapeutic applications.

The migration of skin fibroblast cells is an important aspect of regenerative medicine and wound healing processes.³⁷ Thus, the cell proliferative behaviour of $p(\text{NAG-co-NAPA})_{\text{wc}}$ nanoparticles was studied from the cell viability assay. Furthermore, the pro-migratory effect of $p(\text{NAG-co-NAPA})_{\text{wc}}$ nanoparticles was examined using an *in vitro* wound scratch assay for a period of 0 to 48 h at three different concentrations (62.5 to 250 $\mu\text{g mL}^{-1}$). At three different time points, optical microscopic images were acquired, as shown in Fig. 5(c). It is observed that $p(\text{NAG-co-NAPA})_{\text{wc}}$ nanoparticles can efficiently cover the wounds in L929 cells.

Furthermore, to quantify the wound closure efficiency (%) and wound closure rate (%), Fiji ImageJ software was used.³⁸ After 24 h of incubation of cells with $p(\text{NAG-co-NAPA})_{\text{wc}}$ nanoparticles, $37.84\% \pm 0.06\%$, $68.32\% \pm 0.8\%$ and $80.76\% \pm 0.0009\%$ of the scratched area are filled for the concentrations of 62.5, 125 and 250 $\mu\text{g mL}^{-1}$, respectively. Meanwhile, for the control, $7.55\% \pm 0.06\%$ of the scratch is covered (Fig. 5(d)). After 48 h of incubation, $84.97\% \pm 0.9\%$, $99.56\% \pm 0.3\%$, and $99.94\% \pm 0.007\%$ of the scratched area are covered at the concentrations of 62.5, 125, and 250 $\mu\text{g mL}^{-1}$, respectively. In contrast, for the control, only $49.86\% \pm 0.2\%$ of the scratch is covered (Fig. 5(d)). It was also observed that during the initial 24 h, the wound closure rate (%) is quite fast over all three concentrations as compared to the next 24 h. In the case of the wound closure rate (%), a similar trend is observed (Fig. 5(c)). From 0–24 h and 24–48 h, the wound closure rate is quite fast as compared to 0–48 h. These variations in results are observed due to the contact inhibition and confined space available for the cells to proliferate and migrate. The results obtained from the wound scratch assay demonstrated that $p(\text{NAG-co-NAPA})_{\text{wc}}$ nanoparticles can fill the scratched area ~ 10 times more efficiently compared to the control. From the results of both wound closure (%) and rate of wound closure (%), it is clearly evident that the $p(\text{NAG-co-NAPA})_{\text{wc}}$ nanoparticles show a dose-dependent proliferative and migratory efficiency. Furthermore, it is evident that even at a very low concentration of 62.5 $\mu\text{g mL}^{-1}$, the $p(\text{NAG-co-NAPA})_{\text{wc}}$ nanoparticles can accelerate the wound healing efficiency.

Dose and time-dependent angiogenic nature of $p(\text{NAG-co-NAPA})_{\text{wc}}$ nanoparticles

Angiogenesis plays an important role in the field of wound healing and regenerative medicine. It is a process where the new

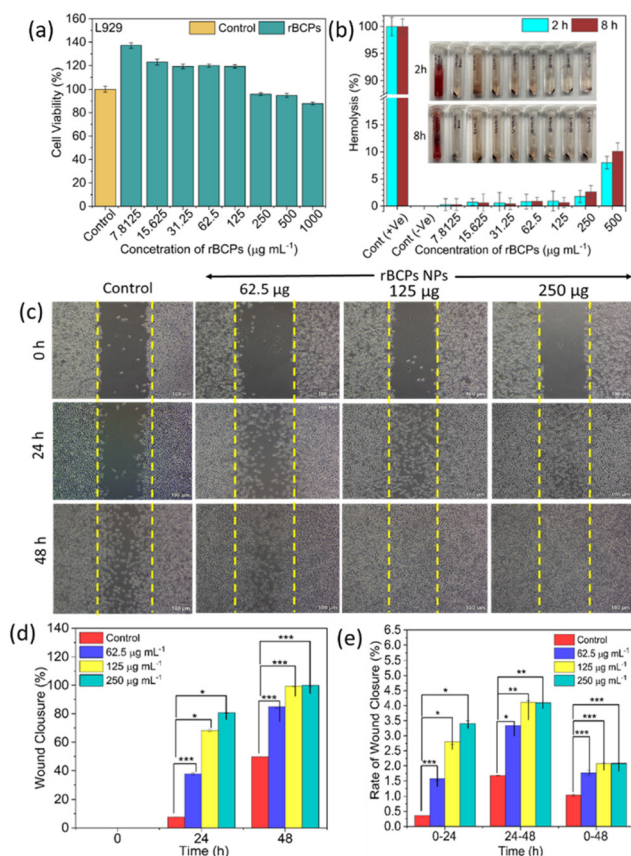


Fig. 5 Biocompatibility, hemocompatibility and proliferation nature of $p(\text{NAG-co-NAPA})_{\text{wc}}$ nanoparticles. (a) Cell viability (%) and (b) hemolysis (%) of $p(\text{NAG-co-NAPA})_{\text{wc}}$ nanoparticles at different concentrations against L929 cells and rat erythrocytes, respectively. The inset image of (b) represents the micro-centrifuge tubes showing hemolysis at 2 h and 8 h. MTT of the $p(\text{NAG-co-NAPA})_{\text{wc}}$ nanoparticles shows no significant difference for both L929, and the hemolysis (%) of the nanoparticles is non-significant with respect to the control (–ve) and significant (*) with respect to the control (+ve) for 2 h and 8 h, respectively. Hemolysis (%) at 500 $\mu\text{g mL}^{-1}$ is significant (**) with respect to the control (–ve) at 8 h. (c) Represents the microscopic images of the wound scratch assay of $p(\text{NAG-co-NAPA})_{\text{wc}}$ at 0, 24 and 48 h taken at 10 \times magnification with a scale bar of 100 μm . (d) and (e) Wound closure (%) and Rate of wound closure (%) of L929. rBCPs represent the $p(\text{NAG-co-NAPA})_{\text{wc}}$ nanoparticles. Data are given as mean \pm SD ($n = 3$) (* $p \leq 0.05$, ** $p \leq 0.05$ –0.01, *** $p \leq 0.05$ –0.001 and ns: non-significant).



blood vessels emerge and/or proliferate from existing blood vessels.³⁹ The results obtained from the cell viability study (Fig. 5(a)) and wound scratch assay (Fig. 5(c–e)) against L929 cells demonstrated that the p(NAG-co-NAPA)_{wc} nanoparticles are proliferative in nature. Furthermore, a chicken embryo membrane assay (CEMA assay) was performed to establish the angiogenic or vascular sprouting nature of the p(NAG-co-NAPA)_{wc} nanoparticles. For this, three different doses (62.5, 125 and 250 µg) of p(NAG-co-NAPA)_{wc} nanoparticles were incubated separately with chick embryos. It is revealed that the presence of p(NAG-co-NAPA)_{wc} nanoparticles causes an increase in the thickness of blood vessels and length (Fig. 6(a)).

To quantify the angiogenic properties, the explant area, vessel area, junction density and mean-E-lacunarity were calculated, as previously mentioned in the experimental section. The explant area corresponds to the overall region where blood vessels are developed. It is observed that compared to the control, at 125 and 250 µg doses, very little explant area has been increased. Meanwhile, for the 62.5 µg dose, an ~80%

increase is observed at 8 h (Fig. 6(b)). A similar result is observed in the case of the vessel area (%). The vessel area describes the total surface area of blood vessels occupied in an explant area. Herein, at a lower dose, the vessel area is increased up to 180% (at 8 h). Meanwhile, for a higher dose, it is increased up to 140% (Fig. 6(c)). In the case of the junction density, a decrease in percentage is observed at a lower dose, while, a slight increase in the junction densities is observed at a higher dose (Fig. 6(d)). The mean-E-lacunarity (%), which indicates the empty spaces available after incubation with the nanoparticles, was also quantified. In the case of a 62.5 µg dose, the mean-E-lacunarity (%) is decreased to 69%; whereas for the control, it is found to be 88% at 8 h. However, upon application of higher doses such as 125 and 250 µg, no such variation in the mean-E-lacunarity (%) is observed (Fig. 6(e)). Based on the time points from 0 to 8 h, for all considered parameters at 62.5 µg dose, it also shows better angiogenic property in nature as compared to the other doses. Thus, the results obtained from the CEMA assay clearly show that the p(NAG-co-NAPA)_{wc} nanoparticles exhibit branching angiogenesis, rather than the sprouting of new blood vessels in a dose and time-dependent manner, where the length and thickness of the developed blood vessels are found to be increased up to 8 h of incubation. These results match well with the previously obtained cell-based studies (Fig. 5), suggesting that p(NAG-co-NAPA)_{wc} nanoparticles are angiogenic in nature at lower doses in a time-dependent manner and are effective for regenerative purposes.

In vivo wound healing efficacy of the p(NAG-co-NAPA)_{wc} nanoformulation

To check the *in vivo* wound healing efficiency of the prepared p(NAG-co-NAPA)_{wc} nanoparticles, a nanoformulation was developed. This nanoformulation was prepared by triturating the p(NAG-co-NAPA)_{wc} nanoparticles with an oleaginous base (see Table S2), as previously described in the method section. To avoid any kind of incongruities, it was examined for phase homogeneity, discolouration and aggregations. It seems to be smooth, consistent and devoid of any aggregation, as observed under white light and *via* touching (Table S3). As the target application is wound healing, an initial skin irritation study was performed with the p(NAG-co-NAPA)_{wc} nanoformulation, oleaginous base, –ve control with no treatment, and +ve control with application of 1% formalin. For the reference, the irritation nature of 1% formalin was also tested with the *in ovo* model for up to 24 h, and the images are shown in Fig. S15. After 48 h of treatment, it is observed that no other groups exhibited skin irritation (Fig. 7(b1), (b3), and (b4)), other than the +ve control group. In the +ve control group, a substantial irritation at the site of application is clearly observed (Fig. 7(b2), black dashed circle). Histology images were acquired from respective rat skin samples (Fig. 7(c–b4)), and demonstrated that in the +ve control group, the damage areas persist in the epidermis layer of skin (Fig. 7(c2), black dashed circle). In contrast, in the other three cases, the layers of skin tissue remain highly intact with no damage. Furthermore, for the

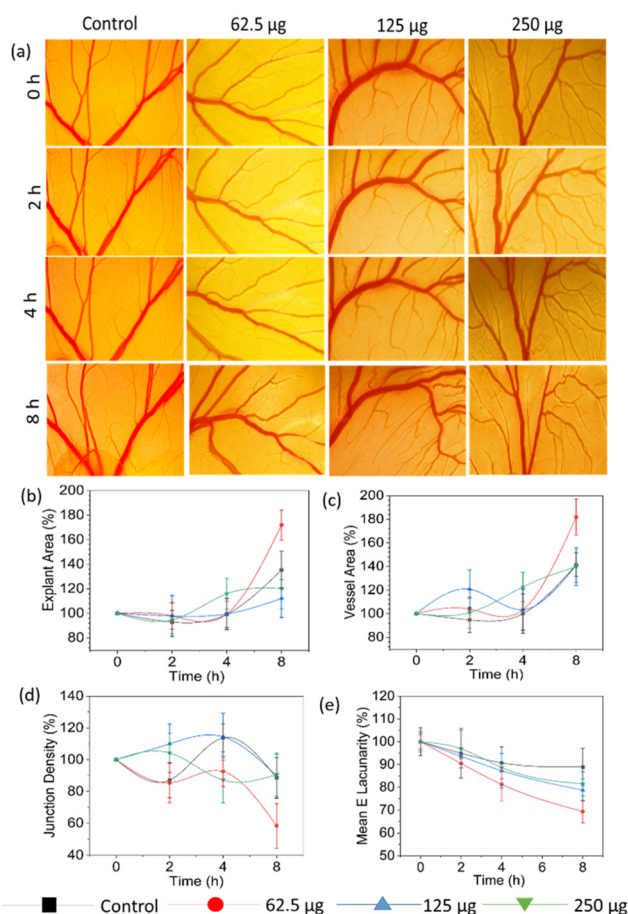


Fig. 6 Angiogenic effect of p(NAG-co-NAPA)_{wc} nanoparticles. (a) *In ovo* CEMA assay in the presence of p(NAG-co-NAPA)_{wc} nanoparticles supports the branching angiogenesis in a dose-dependent manner. (b–e) represent several % changes in the angiogenic parameters such as explant area, vessel area, junction density and mean-E-lacunarity, respectively.



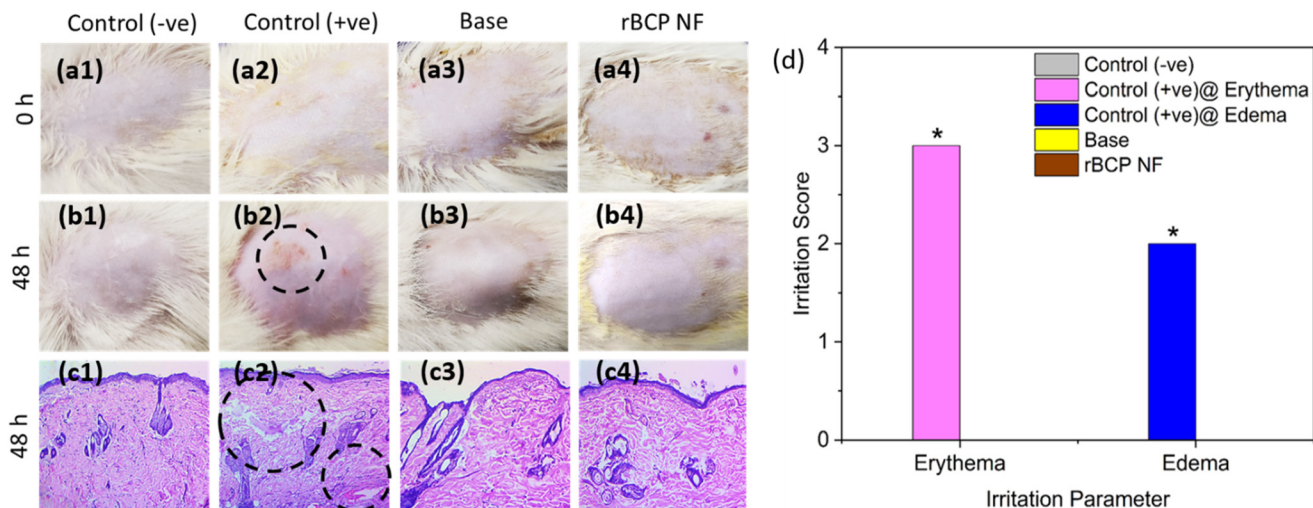


Fig. 7 *In vivo* skin irritation study. (a1–a4) Camera photographs of the skin irritation study captured at 0 h (before treatment) and (b1–b4) at 48 h (after treatment). (c1–c4) Histology images of the H&E staining of tissue samples collected from b1–b4 rat skin at 20× magnification. (d) Calculation of the irritation score based on the occurrence of erythema and edema after 48 h of treatment. The scales for erythema and edema are given in Table S4. rBCP NF represents $p(\text{NAG-co-NAPA})_{\text{wc}}$ nanoparticles-based nanoformulation. Data are given as mean \pm SD ($n = 3$) (* $p \leq 0.05$, ** $p \leq 0.05-0.01$, *** $p \leq 0.05-0.001$ and ns: non-significant).

sensitivity study, the development of erythema and edema is observed. Certain values are assigned to each rat based on the irritation score (Table S4). It was observed that only the +ve control group developed erythema (value = 3) and edema (value = 2) on the skin (Fig. 7(d)). The PDII scores for the +ve control group and other groups were found to be 2 and 0.25, respectively. This signifies that the skin is not irritated or sensitive to the $p(\text{NAG-co-NAPA})_{\text{wc}}$ nanoformulation for up to 48 h. Furthermore, this formulation ensures its use in effective wound healing.

In vivo wound healing experiments were performed on Wistar rats, as mentioned in the methods section. For a clearer understanding, a timeline is provided in Fig. 8(a), which represents the procedure from day 0th (wound creation) to the 15th day after treatment. The impact of the $p(\text{NAG-co-NAPA})_{\text{wc}}$ nanoformulation was assessed, and compared with the control and base (Fig. 8). It can be seen that wound healing is a normal phenomenon of body homeostasis with time. However, from Fig. 8(b1–b15), it is evident that the wound healing progress is swift in the $p(\text{NAG-co-NAPA})_{\text{wc}}$ nanoformulation, followed by base. However, for the control group, it is delayed (Fig. 8(c)). In the control group, complete wound closure is not achieved even after 13 days after treatment. Subsequently, the wound closure rate also increased for the $p(\text{NAG-co-NAPA})_{\text{wc}}$ nanoformulation at least 2–3 days earlier, as compared to the control group. Moreover, the relative wound area (%) was calculated and is shown in Fig. 8(c). The corresponding wound areas (%) are found to be 94.96 ± 2.04 , 86.65 ± 2.03 , and 80.66 ± 1.94 for the control; 51.30 ± 1.63 , 54.98 ± 2.20 , and 30.55 ± 1.36 for the base, and 83.33 ± 4.20 , 54.00 ± 3.96 , and 32.21 ± 3.16 for the $p(\text{NAG-co-NAPA})_{\text{wc}}$ nanoformulation on the 4th, 7th and 10th day after treatment, respectively. Although on the 7th and 10th days after treatment, both the

base and $p(\text{NAG-co-NAPA})_{\text{wc}}$ nanoformulation exhibit similar healed areas (%). However, on the 13th day, it decreases from $12.06\% \pm 4.05\%$ for base to $3.71\% \pm 3.26\%$ for the $p(\text{NAG-co-NAPA})_{\text{wc}}$ nanoformulation group. Particularly, on the 7th day, it is clearly visible from the wounded image of the base (Fig. 8(b8)) that some redness is observed on the skin. This redness may appear due to the inflammation that occurred in the presence of only the base component.

To confirm this phenomenon, further inflammatory markers were examined and they supported our results, which are discussed in the subsequent sections. Additionally, it can be noted from the wounded images (Fig. 8(b1–b15)) that from the 4th day in all groups, wound scabs developed and subsequently prevented the passage of blood and any fluids.⁴⁰ Although this early inflammatory healing stage is observed in all groups, more progress is predominantly observed in the $p(\text{NAG-co-NAPA})_{\text{wc}}$ nanoformulation group, as shown in Fig. 8(b12). As anticipated, on the 7th day of post-treatment, the production of granulation tissue in the $p(\text{NAG-co-NAPA})_{\text{wc}}$ nanoformulation-treated groups is significantly higher in the $p(\text{NAG-co-NAPA})_{\text{wc}}$ nanoformulation group than the control groups. By the 13th day of post-treatment, the wounds in the $p(\text{NAG-co-NAPA})_{\text{wc}}$ nanoformulation group are completely surrounded and covered by fully developed skin layers. In contrast, a significant wound area still remained unhealed in the control group. To support all these findings, a histology study was performed for the tissue samples collected on the 15th day of post-treatment (Fig. 8(b16–b18)). From the images, it is clearly evident that the clumped fibroblasts are generated in the control group. In contrast, in the base and $p(\text{NAG-co-NAPA})_{\text{wc}}$ nanoformulation groups, well-defined dispersed fibroblasts are present. Among the base and $p(\text{NAG-co-NAPA})_{\text{wc}}$ nanoformulation groups, more fibroblasts are present in the



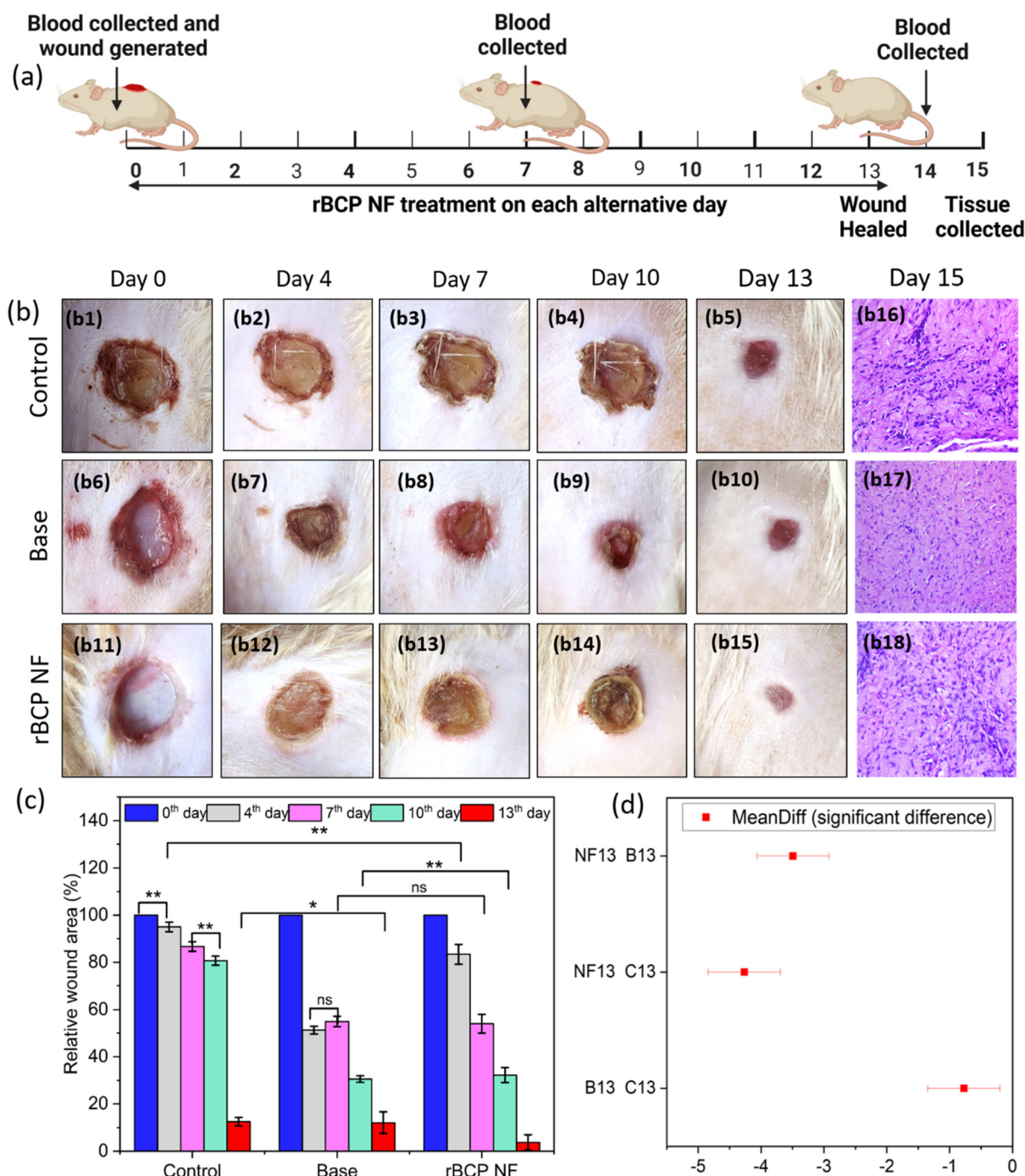


Fig. 8 *In vivo* wound healing results. (a) Timeline of the *in vivo* animal experiment followed in this work. (b) Optical microscopy images of wounds in three different groups (control (b1–b5), base (b6–b10) and rBCP NF (b11–b15)) acquired in high-resolution camera on the 0th, 4th, 7th, 10th and 13th days and (b16–b18) histology images of the H&E staining of healed tissue on the 15th day of post-treatment of the control, base and rBCP NF, respectively, acquired at 20 \times magnification. (c) Relative wound area (%) at five different days (0th, 4th, 7th, 10th and 13th) remaining to heal. (d) Significant differences in mean wound area on the 13th day using the Tukey test to compare the mean between the three different groups. In Fig. 7 (d), C: control group, B: base group and NF: rBCP nanoformulation. Other than the represented statistical significance, all other combinations are significant with $P \leq 0.001$. rBCP NF represents p(NAG-co-NAPA)_{wc} nanoparticles-based nanoformulation. Data are given as mean \pm SD ($n = 3$) (* $P \leq 0.05$, ** $P \leq 0.05-0.01$, *** $P \leq 0.05-0.001$ and ns: non-significant).

wounded area of the p(NAG-co-NAPA)_{wc} nanoformulation group. This increased number of fibroblast cells suggested that on the 15th day of post-treatment, a well-defined skin

layer is formed and the wound is completely covered (Fig. 8 (b18)). The Tukey test was used to compare the means among all groups, and a significant difference was found in the mean

wound area on the 13th day (Fig. 8(d)). Thus, the developed p(NAG-co-NAPA)_{wc} nanoformulation can enhance the wound healing process through angiogenesis (as discussed in the previous section), which helps in repairing and remodelling the tissue by carrying nutrients and oxygen to the wound site.

The levels of cytokine markers were checked using an ELISA KIT on three different phases of wound healing, *i.e.*, inflammatory phase (0th day), proliferative phase (7th day) and remodelling phase (14th day). During these phases of wound healing, the inflammatory markers level changes significantly and they manifest the effectiveness of the applied nanoformulation. It is observed that on the 14th day of post-treatment, the relative levels of TNF- α , IL-1 β and IL-6 are apparently lower than that for the control and base groups (Fig. 9(a-c)). The C-reactive protein (CRP) is generally released from the liver into the bloodstream due to the reaction of inflammatory cytokines. After any injury or damage, the CRP level suddenly increases. With time, as the wound heals, the CRP level decreases. Herein, on the 0th and 14th day of post-treatment, high CRP levels are also observed in the case of the control group as compared to the p(NAG-co-NAPA)_{wc} nanoformulation group (Fig. 9(d)). On the 7th and 14th day of post-treatment, increased levels of IGF-1 are observed for the p(NAG-co-NAPA)_{wc} nanoformulation group, which suggests a higher rate of migration of keratinocytes to the damaged site (Fig. 9(e)).⁴¹ In contrast to the above findings, the base also shows wound healing capacity. On the 7th day of post-treatment, an increased level of pro-inflammatory (TNF- α , IL-1 β and IL-6) markers is observed, as compared to the control group. This deterrent effect is observed due to the inflammation generated by base, and it clearly matches with the images obtained on the 7th day of post-treatment (Fig. 8(b8)). To study the relative fold change in selected gene expressions, an RT-PCR study was conducted, as mentioned in the method section, and is shown in Fig. 9(f) and (g). In this study, GAPDH was used as a house-keeping gene, and the control group's normal and wounded tissue's gene expression values are considered as an internal control for normal and wounded tissues of the base and p(NAG-co-NAPA)_{wc} nanoformulation-treated groups, respectively. RT-PCR studies of 14th day tissue samples revealed that the TNF- α expression level of the wounded tissue is decreased in the base group as compared to that in the normal tissue. However, the IL-1 β expression level is found to be higher in value. This increased IL-1 β expression in the wounded tissue demonstrates that although ~88% of the wound is covered, there is still inflammation present at the wound site. Furthermore, PECAM-1 (CD31) plays a central regulatory role in wound healing and helps in angiogenesis. Compared to normal tissue, PECAM-1 expression is much higher in wounded tissue. In the process of wound healing, VEGF-A (Vascular Endothelial Growth Factor A) contributes both directly and indirectly to the migration of inflammatory cells and keratinocytes. VEGF-A stimulates cell proliferation and collagen deposition in the remodelling phase, and interacts with the KDR receptor (Kinase Insert Domain Receptor), facilitating its internalization into the nucleus. This interaction ultimately

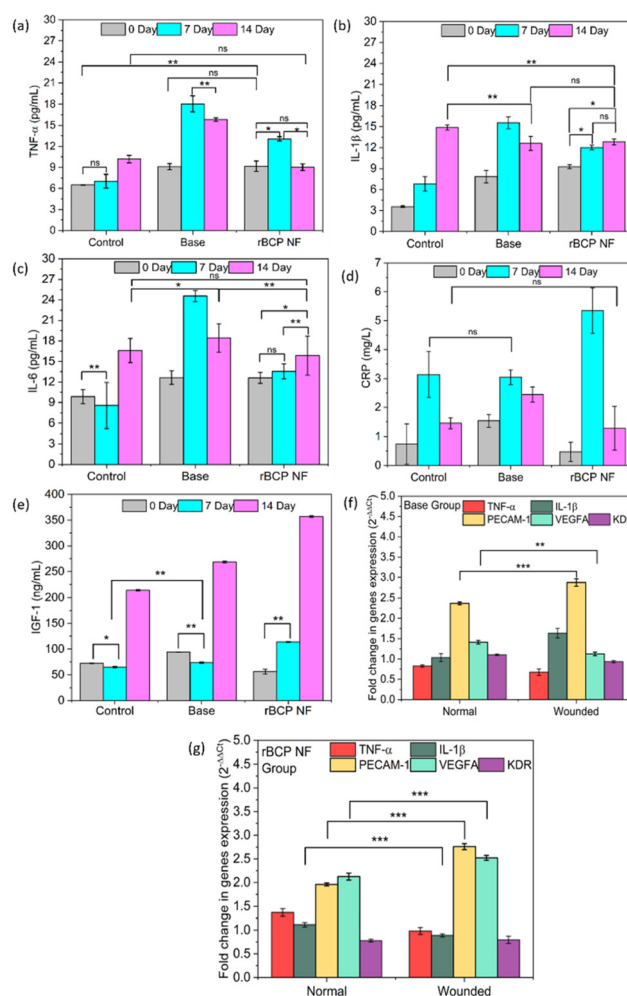


Fig. 9 Wound healing markers and real time expressions of selected genes during *in vivo* wound healing. (a) TNF- α , (b) IL-1 β , (c) IL-6, (d) CRP and (e) IGF-1 levels analysed by ELISA on the 0th day (before wound creation), and the 7th and 14th day. Each data point represents the average \pm SD of three independent determinations ($p < 0.05$). (f) and (g) Relative fold change in gene expressions (TNF- α , IL-1 β , PECAM-1, VEGFA and KDR) obtained from RT-PCR results. Other than the represented statistical significance, all other combinations are significant with $P \leq 0.001$. rBCP NF represents p(NAG-co-NAPA)_{wc} nanoparticles-based nanoformulation. Data are given as mean \pm SD ($n = 3$) (* $P \leq 0.05$, ** $P \leq 0.05-0.01$, *** $P \leq 0.05-0.001$ and ns: non-significant).

leads to the activation of the PI3-kinase/AKT signalling pathway.^{42,43} For wounded tissues, the expression values of VEGFA and KDR are lower with respect to the normal group. However, these changes are statistically non-significant. Furthermore, in the p(NAG-co-NAPA)_{wc} nanoformulation treated groups, a decrease in TNF- α and IL-1 β gene expression values are observed for wounded tissue as compared to the normal tissue. This signifies that the wound is fully covered with no inflammation. For PECAM-1 and VEGFA, an increase in gene expression levels is observed, which is evident from the earlier experiments (Fig. 8(c)). For KDR, no such change in gene expression level is identified. Therefore, it can be



suggested that the $p(\text{NAG-co-NAPA})_{\text{wc}}$ nanoformulation possesses an excellent regulatory effect on TNF- α , IL-1 β , PECAM-1 and VEGFA genes for wound healing and tissue regeneration.

Discussion

In this work, we have synthesized physically crosslinker-free amino acid-based $p(\text{NAG-co-NAPA})_{\text{wc}}$ copolymer nanoparticles with tissue regenerative properties. The synthesis method is based on miniemulsion radical polymerization, which is quite simple and straightforward (Scheme 1). In this synthesis method, we have avoided the use of chemical crosslinkers like DVB or others in order to avoid the toxicity generated due to their presence.^{10,12} The well-designed nanosystems have particle sizes in the submicron range. This ensures their effective interactions with biochemical and cellular components.⁴⁴ From various chemical and physical characterizations, it is confirmed that $p(\text{NAG-co-NAPA})_{\text{wc}}$ nanoparticles were formed with a size range of *ca.* 120–400 nm (Fig. 2(a, b) and (d, e)). From the zeta potential measurement, it is observed that the $p(\text{NAG-co-NAPA})_{\text{wc}}$ nanoparticles are stable as a suspension (Fig. 2(f)). The optical property and secondary structure of the $p(\text{NAG-co-NAPA})_{\text{wc}}$ nanoparticles were investigated using CD spectroscopy, which demonstrated that the $p(\text{NAG-co-NAPA})_{\text{wc}}$ nanoparticles exist in 100% β -turn form (Fig. 2(g)). Furthermore, a distinct separation between the positive and negative bands of the CD spectra (Fig. 2(g)) depicts the formation of a self-assembled structure in the selected medium.²⁸

A detailed MD simulation study has been performed to check the aggregation behaviour of the $p(\text{NAG-co-NAPA})_{\text{wc}}$ nanoparticles at three different temperatures (298, 310, and 315 K). Compared to all three temperatures, particularly at 310 K (physiological temperature), the aggregation of the dimers is found to be quite high. This aggregation behaviour revealed the higher stability of nanoparticles at body temperature (Fig. 3). From MD simulation, it is further revealed that the $p(\text{NAG-co-NAPA})_{\text{wc}}$ nanoparticles are self-assembled where two different regions exist, *i.e.*, hydrophobic and hydrophilic. The hydrophobic region is made up of phenyl rings present in the NAPA unit, and the hydrophilic region is based on the carboxylic acid group present in the NAG unit. The distance between two benzene rings in a hydrophobic region was calculated and found to be in the range of 4.2 to 5.4 Å, which further confirms the existence of π - π interactions between the hydrophobic benzene rings (Scheme 2). It is further confirmed that self-assembled porous $p(\text{NAG-co-NAPA})_{\text{wc}}$ nanoparticles are formed by noncovalent crosslinking, and are due to the π - π interactions or π stacking. Simultaneously, the dynamics of the $p(\text{NAG-co-NAPA})_{\text{wc}}$ nanoparticles have been studied with POPC bilayer membrane, which is an important aspect for *in vivo* studies (Fig. 4(i) and (j)). These interaction studies revealed the biocompatible nature of $p(\text{NAG-co-NAPA})_{\text{wc}}$ nanoparticles. It is important to note that, although a concentrated system was employed in simulations to investigate the struc-

ture and biocompatibility of the $p(\text{NAG-co-NAPA})_{\text{wc}}$ nanoparticles, the results obtained were found to be in good agreement with experimental observations conducted at a diluted concentration [self-assembly behaviour of the nanoparticle (Fig. 3) with good colloidal stability (Fig. 2(f)), and close association of the dimer unit with the POPC bilayer (Fig. 4(j)); *i.e.*, biocompatible nature of the nanoparticle (Fig. 5(a))].

To establish the biomedical applications of $p(\text{NAG-co-NAPA})_{\text{wc}}$ nanoparticles, the cytocompatibility and hemocompatibility of the $p(\text{NAG-co-NAPA})_{\text{wc}}$ nanoparticles have been examined. It was found that the $p(\text{NAG-co-NAPA})_{\text{wc}}$ nanoparticles are proliferative in L929 mouse fibroblast cells up to 1000 $\mu\text{g mL}^{-1}$ (Fig. 5(a)). The hemocompatibility study confirmed that the designed NPs are non-hemolytic in rat erythrocytes as compared to the +ve control (Fig. 5(b)), which means that the $p(\text{NAG-co-NAPA})_{\text{wc}}$ nanoparticles do not interfere with the mechanisms of Na^+/K^+ ATPase and aquaporins.⁴⁵ The migration and proliferation of fibroblasts in the presence of biomaterials are essential processes in the healing of skin wounds. The ability of $p(\text{NAG-co-NAPA})_{\text{wc}}$ nanoparticles to promote both proliferation and migration supports the idea that they aid in re-epithelialization and the restoration of skin functions (Fig. 5(c)).⁴⁶ During acute injury, blood vessel damage leads to nutrient and oxygen shortages in tissues. From the *in ovo* CEMA assay, it was found that the $p(\text{NAG-co-NAPA})_{\text{wc}}$ nanoparticles help to enhance vascular sprouting and angiogenesis, particularly at lower concentrations (Fig. 6). These *in vitro* and *in ovo* results confirm that $p(\text{NAG-co-NAPA})_{\text{wc}}$ nanoparticles can be used in *in vivo* wound healing.

For the *in vivo* study, medical grade materials were used to develop the $p(\text{NAG-co-NAPA})_{\text{wc}}$ nanoformulation and underwent standard quality control tests for preclinical studies, ensuring its suitability for topical applications by adjusting for skin pH using triethanolamine (Table S3). Furthermore, homogeneity and spreadability are crucial for any nanoformulation as a lack of uniformity can lead to secondary injuries by causing delayed healing processes. Therefore, conducting a dermal irritancy test is essential. After applying the formulation, it was assessed for erythema and edema using the Draize scoring scale (Table S4), with results converted into PDII values *via* eqn. (3). The $p(\text{NAG-co-NAPA})_{\text{wc}}$ nanoformulation was applied on rat skin and was compared with the standard irritant, *i.e.*, formalin. Except for the positive control, no rats showed any cutaneous irritation (Fig. 7(b2) and (c2)). Additionally, a period of 7-days observation was carried out for all groups, and none of the animals showed any unusual behaviour. Furthermore, the wound healing capacity of the $p(\text{NAG-co-NAPA})_{\text{wc}}$ nanoformulation was carried out using Wistar rats by generating an 8–10 mm wound on the rats. It is observed that within the 13th day of post-treatment, a major part of the wound is covered as compared to the base and control groups (Fig. 8(b5), (b10) and (b15)). Although the base and $p(\text{NAG-co-NAPA})_{\text{wc}}$ nanoformulation-treated groups show similar extents of wound-covered areas up to the 10th day post-treatment, the whole wound was covered on the 13th day of treatment for the $p(\text{NAG-co-NAPA})_{\text{wc}}$ nanoformulation-treated



groups. These findings match well with the results obtained from the histology study of 14th day old wounds, which demonstrates the formation of dense and dispersed fibroblast cells in the $p(\text{NAG-co-NAPA})_{\text{wc}}$ nanoformulation-treated groups, as compared to the base and control group (Fig. 7 (b18)).^{47,48}

Finally, the study focused on the inflammatory, proliferative and remodelling phases of wound healing, *i.e.*, 0th, 7th and 14th day of treatment, respectively. It was observed that the topically applied $p(\text{NAG-co-NAPA})_{\text{wc}}$ nanoformulation influenced various chemokines, cytokines and growth factors in the systemic blood of both control and treated groups of animals for all three days. The $p(\text{NAG-co-NAPA})_{\text{wc}}$ nanoformulation-treated groups exhibited almost equal levels of TNF- α , IL-1 β and IL-6 (Fig. 8(a-c)), indicating effective anti-inflammatory regulation by $p(\text{NAG-co-NAPA})_{\text{wc}}$. For CRP, a decrease in marker level is also observed on the 14th day of post-treatment for the $p(\text{NAG-co-NAPA})_{\text{wc}}$ nanoformulation-treated groups, which demonstrates that no inflammation persists on the wound site. Meanwhile, for the base, CRP is still higher in value on the 14th day, although the wound is relatively closed as compared to the control group (Fig. 9(d)). By day 14th, IGF-1 levels significantly increased in the treated groups, suggesting enhanced keratinocyte migration towards the wound site (Fig. 9(e)). This rise in IGF-1 values is also correlated with increased vascularity, as it activates the PI3-kinase/Akt signalling pathway and upregulates PDGFB, MMPs and other angiogenic growth factors.²² Additionally, the RT-PCR results of the 14th day tissue samples revealed that compared to those in the base group, the TNF- α and IL-1 β expression levels are lower and the VEGFA and PECAM-1 expression levels are higher in the $p(\text{NAG-co-NAPA})_{\text{wc}}$ nanoformulation-treated groups. This clearly signifies that the $p(\text{NAG-co-NAPA})_{\text{wc}}$ nanoformulation strongly correlates with the regulatory genes related to wound healing and tissue regeneration (Fig. 9(f) and (g)). Hence, it is evident from this work that the self-assembled physically crosslinked $p(\text{NAG-co-NAPA})_{\text{wc}}$ can efficiently act as a potential regenerative medicine.

Conclusions

In summary, we have successfully synthesized novel self-assembled amino acid-based random di-block copolymer nanoparticles of NAG and NAPA, *i.e.*, $p(\text{NAG-co-NAPA})_{\text{wc}}$. Various spectroscopy studies confirmed that $p(\text{NAG-co-NAPA})_{\text{wc}}$ was formed *via* mini-emulsion radical polymerization without the use of any additional covalent crosslinker. The H-bonds from the carboxylic acid groups of NAG and the π - π stacking from the phenyl rings of NAPA triggered non-covalent crosslinking, accelerating the formation of self-assembled spherical $p(\text{NAG-co-NAPA})_{\text{wc}}$ nanoparticles and promoting the construction of a beautiful network-like structure. MD simulation studies also revealed that the $p(\text{NAG-co-NAPA})_{\text{wc}}$ nanoparticles formed aggregates in the temperature range of 298 to 315 K. In aggregates, hydrophobic and hydrophilic groups can

make separate domains and show interactions in close proximity. As anticipated, the hemolysis study and *in vitro* cytotoxicity assay revealed that $p(\text{NAG-co-NAPA})_{\text{wc}}$ nanoparticles are hemocompatible and cytocompatible in nature, respectively. The exciting hallmarks, angiogenesis, cell migration, and proliferation properties established the regenerative property of $p(\text{NAG-co-NAPA})$ nanoparticles. Additionally, *in vivo* experiments demonstrated the potential application of the $p(\text{NAG-co-NAPA})_{\text{wc}}$ nanoformulation in regenerative medicine, *i.e.*, acute wound healing without additional growth factors, such as cytokines, cells, or genes, *etc.* Thus, $p(\text{NAG-co-NAPA})_{\text{wc}}$ nanoparticles are paramount for clinical and therapeutic applications.

Experimental

Materials

All chemicals were used without further purification unless otherwise stated. Glycine (98%, Qualigens), L-phenylalanine methyl ester (Sigma), triethylamine ($\geq 99.5\%$, Merck), 1,4-dioxane (99%) extra pure (Merck), potassium hydroxide (KOH), 2,2'-azo-bis-isobutyronitrile (AIBN, 98%, SRL), SDS (sodium dodecyl sulfate) (90%, Merck), magnesium sulphate anhydrous (SRL), hexadecane anhydrous (HD) (99%, Sigma-Aldrich), (Alfa Aesar), acryloyl chloride stab. with 400 ppm phenothiazine (96%, Alfa Aesar), ethyl acetate, hydrochloric acid, diethyl ether, anhydrous dichloromethane, sodium bisulphate, sodium chloride, toluene, DMSO- d_6 , CDCl_3 , phosphate buffered saline (pH 7.4), isopropanol, phosphotungstic acid, DNS (sodium chloride and dextrose injection IP (0.9% & 5% w/v)) (Jedux), methyl thiazolyltetrazolium (MTT, $>99.9\%$, Himedia), Dulbecco's modified Eagle medium (DMEM, Cell Clone), trypsin-EDTA, 4% paraformaldehyde solution (Himedia), fetal bovine serum (FBS, Gibco), penicillin streptomycin cocktail (Himedia), DMSO (Merck), L929 (mouse fibroblast cells) was acquired from NCCS-Pune repository, India; isoflurane (Abbott), lidocaine (Abbott), white soft paraffin (SRL), paraffin wax (SRL), glycerine (SRL), steryl alcohol (SRL), liquid paraffin (SRL), triethanolamine (Loba Chemie, 98%), hematoxylin (SRL), eosin (Himedia), triazole (Invitrogen), chloroform (Merck) and diethyl polycarbonate treated water (DEPC-treated water, Himedia). Pure Lab Ultra water system (ELGA, High Wycombe, United Kingdom) was used to obtain Ultrapure water (18.2 M Ω cm) for sample processing.

Synthesis of NAG and NAPA monomers

The synthesis of monomers, NAG and NAPA, was performed according to our previously reported approach.^{3,23}

Synthesis of $p(\text{NAG-co-NAPA})_{\text{wc}}$ block copolymer nanoparticles

The synthesis approach of poly[(N-acryloyl glycine)-*co*-(N-acryloyl-(L-phenylalanine methyl ester))] $p(\text{NAG-co-NAPA})_{\text{wc}}$ random block copolymers was quite similar to the procedure used for the synthesis of pNAPA and PNAG with modifications, as reported earlier.^{3,23} In brief, the mixture of two monomers



(NAG and NAPA) with a 1 : 1 ratio was taken by maintaining the total weight at 500 mg. Without DVB and keeping all other parameters fixed, the time for probe sonication was increased to 8.30 minutes, and polymerization was performed. Then, washing with a 1 : 1 ethanol and water mixture was performed 8–10 times, followed by centrifugation (15 000 RPM at 4 °C for 45 minutes), and freeze-drying (48 h) steps to obtain the dried lyophilized white powder. The sample was subsequently stored in a sealed container for further studies.

Characterization of NAG, NAPA, and p(NAG-co-NAPA)_{wc} nanoparticles

The chemical functionalities were confirmed through FT-IR (Fourier transform infrared) spectroscopy (Nicolet iS5, THERMO Electron Scientific Instruments LLC) using the ATR method, and ¹H NMR and ¹³C NMR spectroscopy (500 MHz One Bay NMR spectrometer, BRUKER BioSpin INTERNATIONAL AG). Chemical shifts were recorded in ppm relative to the signals generated by deuterated solvents (DMSO-d₆ for NAG and CDCl₃ for NAPA and p(NAG-co-NAPA)_{wc}), and analysis was performed using MestReNova 15.0. Matrix-assisted laser desorption/ionization-time of flight (MALDI-ToF) mass spectra were measured using a Bruker Autoflex instrument, and the method of analysis was RN_900-4500_Da.par. UV-Vis spectroscopy (Lambda 750 spectrophotometer, PerkinElmer) studies were performed in the range of λ = 190–400 nm. The crystallinity of the polymers was assessed using high-resolution X-ray diffraction (XRD) (Rigaku SmartLab 9 kW powder type (without χ cradle)) in the 2θ = 10°–90° range equipped with Cu K α X-ray source with λ = 1.54 Å. Thermal stability and phase transition of polymers were studied *via* TGA (TGA-50, M s^{−1} Shimadzu (Asia Pacific)) from RT to 600 °C, @ 10 °C min^{−1} heating rate with 100 mL min^{−1} of N₂ gas flow, and DSC (DSC-60 Plus, M s^{−1} Shimadzu (Asia Pacific)) was conducted from 25 °C to 300 °C @ 10 °C min^{−1} heating rate with 100 mL min^{−1} of N₂ gas flow.

Colloidal stability and morphological evaluation

The colloidal stability of the p(NAG-co-NAPA)_{wc} nanoparticles was studied using dynamic light scattering and Zeta sizer (Malvern Zeta Sizer) at 25 °C. DLS and Zeta samples were prepared at 500 μ g mL^{−1} in Milli-Q water. Three acquisitions were recorded, and their average hydrodynamic size and zeta potential values were reported. Circular dichroism (CD, Jasco J-1500 CD spectrometer) measurements were performed in Milli-Q water at four different dilutions at RT, and at three different temperatures with fixed concentration. The spectra were collected from 190 to 300 nm with 0.5 nm data pitch and 1.0 nm bandwidth. For FESEM analysis, ~0.1 mg of p(NAG-co-NAPA)_{wc} nanoparticles was taken in 500 μ L of isopropanol, and bath-sonicated in regular intervals for up to 8 h for uniform dispersion. Then, a few drops of copolymer samples were drop-casted over the cleaned silicon wafer and dried. Images were acquired using Nova NanoSEM 450 equipped with Team Pegasus Integrated EDS-EBSD with Octane Plus and Hikari Pro. For HRTEM analysis, ~0.1 mg of polymer samples were

taken in 500 μ L of isopropanol, and two drops of phosphotungstic acid (PTA) were added. The samples were bath-sonicated in regular intervals for up to 8 h for uniform dispersion. Then, a few drops of polymer samples were drop-casted over the carbon-coated Cu-grid with 200 mesh size, and dried under a tungsten bulb. Images and EDAX patterns were acquired using Tecnai G2 20 TWIN (FEI Company of USA (S.E. A.) PTE, LTD) equipped with TEAM EDS SYSTEM with the Octane Plus SDD detector. For AFM, a sample was prepared in a manner similar to that for FESEM, and images were acquired using NTEGRA Prima.

CMC determination

The CMC was determined using 6-methyl coumarin as a hydrophobic dye based on a previously reported method with slight modification.^{49,50} Once the concentration reached above the CMC, the dye associated with the hydrophobic domain of the p(NAG-co-NAPA)_{wc} nanoparticles and emitted a strong fluorescence. A stock solution of 6 μ M was prepared in dry DCM. Then, 50 μ L of the solution was added to each amber color microcentrifuge tube and kept for 30 minutes in the dark for drying. Subsequently, 400 μ L of p(NAG-co-NAPA)_{wc} nanoparticles in Milli-Q water with different concentrations (1000 μ g mL^{−1} to 0.488 μ g mL^{−1} with 2-fold serial dilutions) was added and the mixture was stirred in the dark at 25 °C for 20 h. Then, the emission spectra were recorded using a microplate reader (Biotek) with λ = 285 nm excitation and λ = 410 nm emission. From the emission *vs.* intensity plot, a tangent was drawn to determine the CMC.

Molecular dynamics simulation

A molecular dynamics simulations study was performed using GROMACS-2020⁵¹ to understand the micro-structure and dynamics of the p(NAG-co-NAPA)_{wc} at different conditions. A CHARMM36⁵² force field was used to model the bonded and non-bonded interactions between the various atoms of the atomistically modelled copolymers and water molecules using the following equation:

$$U_{nb}(r_{ij}) = \sum \frac{q_i q_j}{4\pi\epsilon_0 r_{ij}} + \sum_{i=1}^N 4\epsilon_{ij} \left(\left(\frac{\sigma_{ij}}{r_{ij}} \right)^{12} - 2 \left(\frac{\sigma_{ij}}{r_{ij}} \right)^6 \right) \quad (1)$$

where the non-bonded interactions between i^{th} and j^{th} atoms, having partial charges q , well depth ϵ , distance r , and radius in the Lennard-Jones (LJ) 6–12 term, were used to treat the van der Waals' interaction σ . The bonded interaction energy contributions are bonds, valence angles, dihedral angles, improper dihedral angles, selected Urey–Bradley along with torsional correction map (CMAP) terms, which are further expressed as eqn (2):

$$U_b = \sum_{\text{bonds}} k_b (b - b_0)^2 + \sum_{\text{angles}} k_\theta (\theta - \theta_0)^2 + \sum_{\text{UB}} k_{\text{UB}} (r_{1-3} - r_{1-3,0})^2 + \sum_{\text{dihed}} \sum_{n=1}^N k_n (1 + \cos(n\phi - \delta_n)) + \sum_{\text{imp}} k_\phi (\phi - \phi_0)^2 + \text{CMAP} \quad (2)$$



500 molecules of the co-polymers were randomly placed within the simulation box, considering dimensions of 12 nm × 12 nm × 12 nm. The copolymer molecules were solvated with water, modelled as TIP3P,⁵³ and adequate ions were added to attain 0.15 M NaCl concentration and maintain electroneutrality. To obtain a reasonable starting configuration, the energy of the systems was minimized using the steepest descent algorithm with $F_{\max} < 1000 \text{ kJ mol}^{-1} \text{ nm}^{-1}$. The short-range interaction cut-off for the electrostatics and van der Waal's forces of interaction was taken as 1.2 nm, and the long-range electrostatics were treated using the particle mesh Ewald (PME) method.⁵⁴ Here, similar experimental temperatures (298 K, 310 K and 315 K) and a pressure of 1 atm were maintained during simulations. The temperature and pressure were maintained during simulations using the velocity rescale thermostat with a coupling time of 0.1 ps and the Parrinello-Rahman barostat with a coupling time constant of 2 ps, respectively. The equation of motion was integrated using a leap-frog algorithm, in which the updated position was calculated using a Verlet algorithm^{51,52} (eqn (3) and (4)),

$$r(t + \delta t) = 2r(t) - r(t - \delta t) + \frac{f(t)}{m} (\delta t)^2 + O(\delta t^4) \quad (3)$$

and the updated velocity was calculated at the half-integer time step;

$$v\left(t + \frac{\delta t}{2}\right) = v\left(t - \frac{\delta t}{2}\right) + \frac{f(t)}{m} (\delta t) \quad (4)$$

with a timestep δt of 2 fs.

The production runs were performed for 100 ns, and configurations were stored every 2 ps for further analysis of the structure dynamics. All analyses were performed in GROMACS 2023. 3-Homebrew software.⁵⁵ For all systems, thermodynamic equilibrium was achieved, and the properties calculated are ensemble-averaged over the last 5–20 ns of the trajectory. During the production run, the variation of the different thermodynamic and structural parameters is shown against time, as shown in Fig. S14. The properties of interest for describing the copolymer system include the radial distribution function (RDF), hydrogen bonding (HB), solvent-accessible surface area (SASA), mean square displacement (MSD) and number of contact groups. The visual inspection of the simulation results was carried out using VMD 1.9.4.⁵⁶ To ensure the reliability of the obtained results and statistical significance, all the simulations were run three times. The topology file for the copolymer system has been provided in Fig. S9. The description of the systems is shown in Table S1.

In vitro cell viability study through MTT assay

The cell viability of the p(NAG-co-NAPA)_{wc} nanoparticles was evaluated using the healthy cell line L929, which is a mouse fibroblast cell line. Cells were cultured in 10% of FBS-supplemented DMEM with 100 U of penicillin-streptomycin antibiotic (complete media) and maintained in an incubator at 37 °C with 5% CO₂. 1×10^4 cells per well were cultured in a

96-well plate for up to 24 h, followed by the addition of different concentrations of p(NAG-co-NAPA)_{wc} nanoparticles ($1000 \mu\text{g mL}^{-1}$ to $7.9 \mu\text{g mL}^{-1}$ with 2-fold serial dilution). After 24 h of incubation, samples were removed. Then, $5 \mu\text{g mL}^{-1}$ of MTT reagent prepared in fresh media was added to each well and incubated for 4 h. The MTT reagent was removed and 100 μL of DMSO was subsequently added per well, and the samples were again incubated for 20 minutes in the dark. Finally, the absorbance was recorded at $\lambda_{\max} = 570 \text{ nm}$ using a microplate reader (Biotek, SYNERGY H1M). The cell viability (%) was calculated using eqn (5). Data were collected in three distinct biological replicates; each performed on a different day with different cell passages and three repetitions.

$$\text{Cell viability (\%)} = \frac{\text{OD}_{(\text{treatment})}}{\text{OD}_{(\text{control})}} \times 100 \quad (5)$$

Hemolysis study

Hemolysis was conducted on RBCs collected from rat's whole blood. In brief, blood samples were collected by rat cardiac puncture, washed/centrifuged (3500 RPM, 5 min, RT), and then homogenized to get a uniform suspension of RBCs in sterile DNS (5×10^6 cells per μL). To determine the hemolytic effect of polymeric nanoparticles, RBCs were incubated with different concentrations of p(NAG-co-NAPA)_{wc} ($500 \mu\text{g mL}^{-1}$ to $7.8125 \mu\text{g mL}^{-1}$ with a dilution factor 2) for 2 h and 8 h at 37 °C with 100 RPM. Incubation with DNS and distilled water were considered as the negative and positive controls, respectively. After incubation, at particular intervals, samples were centrifuged at 3500 RPM for 5 minutes at RT, the supernatant was collected and absorbance was recorded at $\lambda_{\max} = 540 \text{ nm}$, and the % hemolysis was estimated using eqn (6). Experiments were performed with the same rat blood in three distinct tubes for each concentration of p(NAG-co-NAPA)_{wc} nanoparticles.

$$\begin{aligned} \text{Hemolysis (\%)} &= \frac{\text{OD}_{(\text{treatment})}}{\text{OD}_{(\text{negative control})} / \text{OD}_{(\text{positive control})}} \\ &= \text{OD}_{(\text{negative control})} \times 100 \end{aligned} \quad (6)$$

In vitro wound scratch assay

The wound scratch assay *in vitro* was performed to check the cell proliferation and migration properties of the p(NAG-co-NAPA)_{wc} nanoparticles on a two-dimensional scale. This assay was performed with L929 cells. 2×10^5 cells per well of 12-well plates with 800 μL complete media were taken, and incubated for 24 h for 70%–80% confluency with adhesion. Then, a linear scratch wound was generated for each well by using a 20 μL sterile tip, followed by washing with 1X PBS three times. Then, the desired concentrations of p(NAG-co-NAPA)_{wc} nanoparticles ($250 \mu\text{g mL}^{-1}$ to $62.5 \mu\text{g mL}^{-1}$) were added to the wells. Further images were acquired at 0, 24 and 48 h. Closing wound area (%) and closing rate (%) were calculated using Fiji ImageJ Software.



Chicken embryo membrane assay (CEMA)

Fertilized chicken eggs were purchased from a trusted and certified vendor (Ramana Hatchery, Varanasi, Uttar Pradesh, India) and incubated in an egg incubator (37 °C, 50%–55% RH) for up to 4 days before the experiment. On the day of the experiment, using a light-shadow approach, the eggs were tested to check whether embryogenesis had occurred or not. Then, 1–2 mL of albumen was removed for the detachment of the developed chick embryo chorioallantoic membrane, and a small window was created on the top of the eggshell. Different concentrations of p(NAG-co-NAPA)_{wc} nanoparticles were prepared in PBS 7.41 (250, 125 and 62.5 µg), with PBS as the control, and added and examined for up to 24 h. The images were captured at different time intervals (0, 2, 4, and 8 h) using a stereo zoom microscope-mounted Magnus camera (Magcam DC Plus 10, Magnus Opto Systems India Pvt. Ltd) at a resolution of 10 megapixels, and analysed using the Angio tool and Fiji ImageJ software.

Development of p(NAG-co-NAPA)_{wc} nanoformulation and macroscopic evaluation

The p(NAG-co-NAPA)_{wc} nanoformulation was prepared by disseminating p(NAG-co-NAPA)_{wc} nanoparticles (1% w/w) with an oleaginous base to facilitate smooth application on the wounds. The composition of the oleaginous base is given in Table S2. The p(NAG-co-NAPA)_{wc} nanoparticles were initially dispersed on the ointment slab, followed by trituration with base by using a long, broad spatula. Glycerine was added last after complete trituration of the ointment with the base. Then, the p(NAG-co-NAPA)_{wc} nanoformulation was stored in an open-mouth airtight container at RT. The nanoformulation was further used for macroscopic qualitative assessment. The parameters considered for macroscopic evaluation are given in Table S3.

Biological evaluation of the p(NAG-co-NAPA)_{wc} nanoformulation

Ethical approval. All animal experiments were carried out in accordance with the guidelines of CPCSEA, and approved by the Institutional Animal Ethical Committee (IAEC) of IIT (BHU), Varanasi, Uttar Pradesh, India (Regd. no. 2123/GO/Re/S/21/CPCSEA). The animal ethical approval reference No. is IIT (BHU)/IAEC/2023/048 and Patent Application No. (202511043769).

In vivo skin irritation and sensitization

To check for any type of irritation and erythematous reactions, the p(NAG-co-NAPA)_{wc} nanoformulation was applied on the Wistar rat's skin and observed for 48 h. For this study, ~4 cm² rat skin was shaved, and the p(NAG-co-NAPA)_{wc} nanoformulation was applied with formalin (a common irritant) considered as a control. The treated area was wrapped with a bandage and kept for 48 h. After 48 h, bandages were removed, washed with sufficient amounts of water, and visually examined for any kind of irritation and sensitization. Additionally, high-resolu-

tion images were captured and compared with images acquired before treatment. Furthermore, the examined rats were kept under observation to check for edema and erythema. To calculate the skin irritation score, the Draize scoring system^{57–59} (Table S4) was used with the primary dermal irritation index (PDII) through eqn (7). Further tissue samples were collected for histology:

$$\text{PDII} = \text{PDI}/4 \quad (7)$$

where '0' indicates no irritation, 0.5–1.9 indicates modest discomfort, 2–4.9 indicates mild irritation, and values above 5 indicate severe irritation.

In vivo wound healing

The treatment efficiency of the p(NAG-co-NAPA)_{wc} nanoformulation for wound healing was evaluated using Wistar rats. Initially, 3% isoflurane was used to anesthetize the rats, followed by the removal of hairs at the back using a trimmer. Then, lidocaine, a local anaesthetic, was applied at the target site. An 8–10 mm full-thickness cutaneous wound was generated at the shaved site by using a sterile 8 mm biopsy punch. The wound region was cleaned with sterile cotton and topically treated with ~50–60 mg of p(NAG-co-NAPA)_{wc} nanoformulation on each alternative day (0th to 12th, once in each alternative day). Wounded regions were covered with a conventional sterile gauze bandage. The dressing was replaced with a fresh bandage after each treatment. Similar steps were followed for the control group for the base as well.

Study of histology and immunochemical assay

For the histology study, deep granulation tissue and cross-sectional full-thickness skin specimens were collected on the 15th day post-treatment from the cicatricial tissue. Then, specimens were fixed and embedded in formalin and paraffin wax. Blocks were further sectioned with a thickness of 5 µm in the transverse plane. The sections were stained with hematoxylin and eosin, then mounted on glass slides and subsequently analysed using an optical microscope at 20× magnification. For immunochemical analysis, the blood serum sample was isolated from rats. The blood samples were collected on three different days (0th, 7th and 14th day), which represented distinct phases of the wound healing cycle and were stored at –80 °C for further processing. Then, the levels of Immune markers such as IL-1β, IL-6, CRP, TNF-α and IGF-1 were estimated using commercially available enzyme-linked immunosorbent assay (ELISA) kits, as per the instruction. The relative protein concentrations were estimated by recording the absorbance at λ_{max} = 450 nm and compared with the control samples.

Reverse transcription and polymerase chain reaction (RT-PCR)

On the 14th day of post-treatment, nearly 1 mm thickness of tissues was collected from the excised wounds and also from the normal skin of all the groups. RNA was isolated by homogenizing tissue samples in 1 mL of TRIAZOL reagent, fol-



lowed by chloroform extraction. The aqueous layer was collected, and RNAs were precipitated in 1 mL of isopropyl alcohol and centrifuged (12 000g) at 4 °C for 15 minutes. The RNA pellets were washed with 70% ice-cold ethanol for 2 times and suspended in DEPC-treated water. Afterward, RNA was quantified. Then, 1 µg of RNA sample was used for cDNA synthesis using oligo dT sequence and reverse transcriptase polymerase, as per the manufacturer's protocol.

RT-PCR (QuantStudio 5, Applied Biosystems) was set up using diluted cDNA samples (1 : 100) in a final volume of 20 µL with the PowerUp™ SYBR™ GREEN Master Mix (Invitrogen) and different optimized concentrations of KiCqStart® primers (Sigma) for biomarker target genes, such as KDR(5'-AACTGGATAAAATGGGCG-3') and (3'-AGCCTTTTGGTAGAGTCAG-5'), VEGFA(5'-CTCATCTCTCCTATGTGCTG-3') and (3'-GATAGAGTATATCTTCAAGCCG-5'), PECAM-1 (5'-AAACCACAATTGAGTACCAG-3') and (3'-ACTTAGCTTGACGTTCTTTG-5'), IL-1β (5'-GGATGATGATGATAACCTGC-3') and (3'-CATGGAGAATATCATTGTTGG-5'), TNF-α (5'-CTATGTCTCAGCCTCTTCTC-3') and (3'-CATTTGCCAAGTGGCCATCC-5') and GAPDH (5'-TCGGAGTCAACGGATTTG-3') and (3'-GAGACATTTACCTATAACAAC-5') as housekeeping genes, using Taq polymerase (TAKARA R001A) with 40 repetitive cycles of denaturation at 95 °C for 25 s, annealing for 30 s at 60 °C, extension at 72 °C for 35 s and final extension for 7 minutes at 72 °C. RT-PCR experiments were performed in triplicate for all samples along with the control. The fold change in selected gene expressions with respect to the control was calculated using the comparative Ct method.⁵⁸

Statistical significance

One-way ANOVA with Tukey test and independent Student's *t*-test were used to statistically evaluate the *in vitro* and *in vivo* data using Origin software (OriginLab Corporation, Northampton, USA). The statistical significance in comparison groups was calculated by considering *p* < 0.05. The data are represented as a mean of ±SD or unless otherwise stated.

Author contributions

P. P. and D. B. are the principal investigators (PI) of this project. The ideation, experimental designs, result analysis, and manuscript writing were mainly carried out by S. P. and P. P., D. B. and D. D. Y. contributed to the MD simulation, and G. S., P. S. S., and A. S. K. assisted with the *in vivo* study. Jyotirmayee assisted with the RT-PCR study. D. P. helped perform the *in vivo* irritation study, and A. R. M. contributed to the design of the schemes. The manuscript was written and finalized by S. P., D. B., and P. P. All authors reviewed and approved the final version for submission.

Conflicts of interest

The authors declare no competing financial interests.

Data availability

The datasets generated during experiments, computational studies and/or analysis for this article are available from the authors/communicating authors on reasonable request.

NMR (¹H and ¹³C) of monomers, FTIR of monomers, ¹³C NMR, UV-Vis, MALDI-ToF, DLS of the copolymer, CD report generated from instrument, topology file used for MD simulation, aggregation behavior of hydrophobic unit and hydrophilic units in three different temperatures, angle distribution between Ph14-Ph14 at three concerned temperatures, number of Hydrogen bonds and number of contacts in between copolymer and water, thermodynamic equilibrium properties of NAG-NAPA dimer system and microscopic images of CAM assay studied for formalin; table representing system description used for MD simulation, ingredient (%) of oleagenous base, qualitative assessment of oleagenous base and nanoformulation and skin irritation value based on Draize score. See DOI: <https://doi.org/10.1039/d5nr00281h>.

Acknowledgements

The authors acknowledge financial support awarded to Prof. Paik by I-DAPT (File no. I-DAPT/IT (BHU)/2023-24/Project Sanction/47), Indian Council of Medical Research (ICMR), India (Ref: EMDR/SG/12/2023-4724), STARS-IISc Bangalore (Ref. MoE-STARS/STARS-2/2023-0318), and Anusandhan National Research Foundation, India (Ref: CRG/2023/005576). Sukanya is grateful for the DST-INSPIRE fellowship (IF180185) award and financial support from ICMR to carry out the Ph.D. work. The authors also acknowledge the start-up company Triphan Healthcare Pvt. Ltd, at I3F, IIT(BHU), Varanasi, India, for instrumental support. The authors acknowledge Dr Avanish Singh Parmar (Department of Physics, IIT (BHU)) for the Zeta Analyser. The Param Shivay Supercomputing Facility at IIT (BHU), Varanasi, funded by MeitY under the National Supercomputing Mission, was used to conduct the MD simulations.

References

- O. J. Deane, J. Jennings and S. P. Armes, *Chem. Sci.*, 2021, **12**, 13719–13729.
- H. Sun, D. Liu and J. Du, *Chem. Sci.*, 2019, **10**, 657–664.
- A. K. Yamala, V. Nadella, Y. Mastai, H. Prakash and P. Paik, *Nanoscale*, 2017, **9**, 14006–14014.
- A. K. Yamala, V. Nadella, Y. Mastai, H. Prakash and P. Paik, *J. Appl. Polym. Sci.*, 2020, **137**, 48363.
- Y. Que, Y. Liu, W. Tan, C. Feng, P. Shi, Y. Li and H. Xiaoyu, *ACS Macro Lett.*, 2016, **5**, 168–173.
- X. Liu, Q. Su, J. Zhu and X. Song, *Polymers*, 2023, **15**, 2490.



- 7 M. Talelli, M. Barz, C. J. F. Rijcken, F. Kiessling, W. E. Hennink and T. Lammers, *Nano Today*, 2015, **10**, 93–117.
- 8 C. Deng, Y. Jiang, R. Cheng, F. Meng and Z. Zhong, *Nano Today*, 2012, **7**, 467–480.
- 9 C. H. Jeong, D. H. Kim, J. H. Yune, H. C. Kwon, D.-M. Shin, H. Sohn, K. H. Lee, B. Choi, E. S. Kim, J. H. Kang, E. K. Kim and S. G. Han, *Toxicol. in Vitro*, 2021, **70**, 105034.
- 10 M. Hanson and A. Wypych, in *Databook of Curatives and Crosslinkers*, ed. M. Hanson and A. Wypych, ChemTec Publishing, 2019, pp. 1–2, DOI: [10.1016/B978-1-927885-49-9.50003-7](https://doi.org/10.1016/B978-1-927885-49-9.50003-7).
- 11 J. Chen, E. S. Garcia and S. C. Zimmerman, *Acc. Chem. Res.*, 2020, **53**, 1244–1256.
- 12 C. Amgoth, G. Dharmapuri, S. Patra, K. Wasnik, P. Gupta, A. M. Kalle and P. Paik, *J. Appl. Polym. Sci.*, 2021, **138**, 50386.
- 13 Y. Shao, W. Huang, C. Shi, S. T. Atkinson and J. Luo, *Ther. Delivery*, 2012, **3**, 1409–1427.
- 14 S. Buwalda, A. Al Samad, A. El Jundi, A. Bethry, Y. Bakkour, J. Coudane and B. Nottelet, *J. Colloid Interface Sci.*, 2018, **514**, 468–478.
- 15 Q. Hu, C. J. F. Rijcken, E. van Gaal, P. Brundel, H. Kostkova, T. Etrych, B. Weber, M. Barz, F. Kiessling, J. Prakash, G. Storm, W. E. Hennink and T. Lammers, *J. Controlled Release*, 2016, **244**, 314–325.
- 16 M. Lin, Y. Dai, F. Xia and X. Zhang, *Mater. Sci. Eng., C*, 2021, **119**, 111626.
- 17 J. Chen, B. Yan, X. Wang, Q. Huang, T. Thundat and H. Zeng, *Polym. Chem.*, 2017, **8**, 3066–3073.
- 18 G. Wu, C. Li, X. Liu, J. Lv, Y. Ding, Y. Liu, Y. Liu, F. Huang, L. Shi, Y. An and R. Ma, *Colloids Surf., B*, 2019, **180**, 376–383.
- 19 W.-R. Zhuang, Y. Wang, P.-F. Cui, L. Xing, J. Lee, D. Kim, H.-L. Jiang and Y.-K. Oh, *J. Controlled Release*, 2019, **294**, 311–326.
- 20 H. Hosseinkhani, P.-D. Hong and D.-S. Yu, *Chem. Rev.*, 2013, **113**, 4837–4861.
- 21 D. W. P. M. Löwik and J. C. M. van Hest, *Chem. Soc. Rev.*, 2004, **33**, 234–245.
- 22 P. S. Gupta, K. Wasnik, S. Patra, D. Pareek, G. Singh, D. D. Yadav, S. Maity and P. Paik, *Nanoscale*, 2024, **16**, 1770–1791.
- 23 P. S. Gupta, K. Wasnik, G. Singh, S. Patra, D. Pareek, D. D. Yadav, M. S. Tomar, S. Maiti, M. Singh and P. Paik, *Mater. Adv.*, 2023, **4**, 4718–4731.
- 24 C. A. Hunter and J. K. M. Sanders, *J. Am. Chem. Soc.*, 1990, **112**, 5525–5534.
- 25 J. Jiang, O. V. Lima, Y. Pei, Z. Jiang, Z. Chen, C. Yu, J. Wang, X. C. Zeng, E. Forsythe and L. Tan, *ACS Nano*, 2010, **4**, 3773–3780.
- 26 H. S. Purohit, N. S. Trasi, D. D. Sun, E. C. Y. Chow, H. Wen, X. Zhang, Y. Gao and L. S. Taylor, *J. Pharm. Sci.*, 2018, **107**, 1330–1341.
- 27 A. Schittny, J. Huwyler and M. Puchkov, *Drug Delivery*, 2020, **27**, 110–127.
- 28 L. Werber, L. C. Preiss, K. Landfester, R. Muñoz-Espí and Y. Mastai, *Chirality*, 2015, **27**, 613–618.
- 29 N. Amdursky and M. M. Stevens, *ChemPhysChem*, 2015, **16**, 2768–2774.
- 30 L. Adler-Abramovich, L. Vaks, O. Carny, D. Trudler, A. Magno, A. Caflisch, D. Frenkel and E. Gazit, *Nat. Chem. Biol.*, 2012, **8**, 701–706.
- 31 Y. Lu, E. Zhang, J. Yang and Z. Cao, *Nano Res.*, 2018, **11**, 4985–4998.
- 32 S. Kim, Y. Shi, J. Y. Kim, K. Park and J.-X. Cheng, *Expert Opin. Drug Delivery*, 2010, **7**, 49–62.
- 33 E. Rideau, R. Dimova, P. Schwill, F. R. Wurm and K. Landfester, *Chem. Soc. Rev.*, 2018, **47**, 8572–8610.
- 34 S. Avsar, M. Kyropoulou, S. Di Leone, C.-A. Schoenenberger, W. P. Meier and C. G. Palivan, *Front. Chem.*, 2019, **6**, 645.
- 35 Y. Zhao, J. Li, H. Gu, D. Wei, Y.-c. Xu, W. Fu and Z. Yu, *Interdiscip. Sci.:Comput. Life Sci.*, 2015, **7**, 211–220.
- 36 O. Maksimenko, J. Malinovskaya, E. Shipulo, N. Osipova, V. Razzhivina, D. Arantseva, O. Yarovaya, U. Mostovaya, A. Khalansky, V. Fedoseeva, A. Alekseeva, L. Vanchugova, M. Gorshkova, E. Kovalenko, V. Balabanyan, P. Melnikov, V. Baklaushev, V. Chekhonin, J. Kreuter and S. Gelperina, *Int. J. Pharm.*, 2019, **572**, 118733.
- 37 S. Cometa, C. Licini, M. A. Bonifacio, P. Mastroilli, M. Mattioli-Belmonte and E. De Giglio, *Carbohydr. Polym.*, 2022, **283**, 119145.
- 38 E. Zudaire, L. Gambardella, C. Kurcz and S. Vermeren, *PLoS One*, 2011, **6**, e27385.
- 39 R. Li, K. Liu, X. Huang, D. Li, J. Ding, B. Liu and X. Chen, *Adv. Sci.*, 2022, **9**, 2105152.
- 40 G. S. Schultz, G. A. Chin, L. Moldawer and R. F. Diegelmann, *Mechanisms of vascular disease: A reference book for vascular specialists [Internet]*, 2011.
- 41 P. Deng, L. Yao, J. Chen, Z. Tang and J. Zhou, *Carbohydr. Polym.*, 2022, **276**, 118718.
- 42 T. A. Wilgus, *Adv. Wound Care*, 2018, **8**, 671–678.
- 43 I. Domingues, J. Rino, J. A. A. Demmers, P. de Lanerolle and S. C. R. Santos, *PLoS One*, 2011, **6**, e25668.
- 44 M. Moreno-Sastre, M. Pastor, A. Esquisabel, E. Sans, M. Viñas, D. Bachiller and J. L. Pedraz, *J. Microencapsulation*, 2016, **33**, 636–645.
- 45 I. Greco, N. Molchanova, E. Holmedal, H. Jenssen, B. D. Hummel, J. L. Watts, J. Håkansson, P. R. Hansen and J. Svenson, *Sci. Rep.*, 2020, **10**, 13206.
- 46 G. Han, L. N. Nguyen, C. Macherla, Y. Chi, J. M. Friedman, J. D. Nosanchuk and L. R. Martinez, *Am. J. Pathol.*, 2012, **180**, 1465–1473.
- 47 H. Rostami, R. Mohammadi, S. Asri-Rezaei and A. A. Tehrani, *Iran. J. Vet. Surg.*, 2018, **13**, 14–22.
- 48 T. Kardan, R. Mohammadi, S. Taghavifar, M. Cheraghi, A. Yahoo and K. Mohammadnejad, *Int. J. Low Extrem. Wounds*, 2021, **20**, 263–271.



- 49 H. Su, F. Wang, W. Ran, W. Zhang, W. Dai, H. Wang, C. F. Anderson, Z. Wang, C. Zheng, P. Zhang, Y. Li and H. Cui, *Proc. Natl. Acad. Sci. U. S. A.*, 2020, **117**, 4518–4526.
- 50 A. Fluksman and O. Benny, *Anal. Methods*, 2019, **11**, 3810–3818.
- 51 H. Bekker, H. Berendsen, E. J. Dijkstra, S. Achterop, R. Drunen, D. van der Spoel, A. Sijbers, H. Keegstra, B. Reitsma and M. K. R. Renardus, *Phys. Comput.*, 1993, **92**, 252–256.
- 52 A. Croitoru, S.-J. Park, A. Kumar, J. Lee, W. Im, A. D. MacKerell Jr. and A. Aleksandrov, *J. Chem. Theory Comput.*, 2021, **17**, 3554–3570.
- 53 P. Mark and L. Nilsson, *J. Phys. Chem. A*, 2001, **105**, 9954–9960.
- 54 T. Darden, D. York and L. Pedersen, *J. Chem. Phys.*, 1993, **98**, 10089–10092.
- 55 Homebrew Formulae, <https://formulae.brew.sh/formula/gromacs>, (accessed 24-07-2024, 2024).
- 56 W. Humphrey, A. Dalke and K. Schulten, *J. Mol. Graphics*, 1996, **14**, 33–38, 27–38.
- 57 Z. Djerrou, H. Djaalab, F. Riachi, M. Serakta, A. Chettou, Z. Maameri, B. Boutobza and Y. Hamdi-Pacha, *Afr. J. Tradit., Complementary Altern. Med.*, 2013, **10**, 480–489.
- 58 M. S. Latif, A. Nawaz, S. A. Rashid, M. Akhlaq, A. Iqbal, M. J. Khan, M. S. Khan, V. Lim and M. Alfatama, *Polymers*, 2022, **14**, 2211.
- 59 M. W. Pfaffl, *Nucleic Acids Res.*, 2001, **29**, e45.

